Flow field-based data analysis in interfacial shear rheometry

Pablo Sánchez-Puga[a,*], Javier Tajuelo[b], Juan Manuel Pastor[c], Miguel A. Rubio[a]

[a] *Departamento de Física Fundamental, Facultad de Ciencias, Universidad Nacional de Educación a Distancia, UNED, 28040 Madrid, Spain*
[b] *Departamento de Física Interdisciplinar, Facultad de Ciencias, Universidad Nacional de Educación a Distancia, UNED, 28040 Madrid, Spain*
[c] *Complex System Group (ETSIAAB), Universidad Politécnica de Madrid, 28040 Madrid, Spain*

Abstract

Developments in interfacial shear rheometers have considerably improved the quality of experimental data. However, data analysis in interfacial shear rheometry is still an active field of research and development due to the intrinsic complexity introduced by the unavoidable contact of the interface with, at least, one supporting bulk subphase. Nonlinear velocity profiles, both at the interface and the bulk phases, pervade the system dynamical behavior in the most usual experimental geometries, particularly in the case of soft interfaces. Such flow configurations demand data analysis schemes based on the explicit calculation of the flow field in both the interface and the bulk phases. Such procedures are progressively becoming popular in this context.

In this review, we discuss the most recent advances in interfacial shear rheology data analysis techniques. We extensively review some recently proposed flow field-based data analysis schemes for the three most common interfacial shear rheometer geometries (magnetic needle, double wall-ring, and bicone), showing under what circumstances the calculation of the flow field is mandatory for a proper analysis of the experimental data. All cases are discussed starting at the appropriate hydrodynamical models and using

*Corresponding author.
E-mail address: p.sanchez@fisfun.uned.es

the equation of motion of the probe to set up an iterative procedure to compute the value of the complex Boussinesq number and, from it, the complex interfacial viscosity or, equivalently, the complex interfacial modulus. Moreover, two examples of further extensions of such techniques are proposed, concerning the micro-button interfacial shear rheometer and the potential application of interfacial rheometry instruments, together with adapted flow field-based data analysis techniques, for bulk rheometry, particularly in the case of soft samples.

Keywords: Interfacial Shear Rheology, Flow Field approximations, Finite differences, Bicone, Magnetic Tweezers, Microwires, DWR, Microrheology, Langmuir Monolayers, Surfactants

---

Highlights:

- Flow field-based data analysis techniques can handle the pervading nonlinear interfacial and bulk velocity profiles appearing at moderate and low interfacial viscosities in the usual interfacial rheometer geometries.
- Flow field-based data analysis techniques allow for a more accurate separation of the interfacial and bulk phase drags, and a more precise calculation of the elastic and viscous components of the response.
- With modern microprocessors and mathematical platforms, flow field-based techniques can be implemented in real-time control and measurement software of interfacial rheometric systems.
- The application of geometries designed for interfacial rheometry (DWR, MNISR, bicone) together with flow field-based techniques in the study of the bulk rheology of soft materials appears to be very promising.

1. Introduction

Shear flow and deformation properties of bulk and interfacial systems are active fields of research because of their importance from applied and basic points of view [1, 2, 3, 4, 5, 6]. However, the translation of rheological experimental data into rheometric parameters values is far from trivial because the process typically involves three coupled ingredients: the experimental system (comprising both the sample and the instrument's hardware and software), the fluid-dynamical problem (including the equations of the sample and probe dynamics and the boundary conditions), and the rheological model of the sample.

In shear oscillatory tests, the rheological model is usually quite simple because it is typically assumed that the viscoelastic properties of the sample can be represented by a dynamic modulus, G^*, that relates stresses to deformations. Moreover, the dynamic modulus is usually represented as a complex function of the oscillation frequency, ω, so that $G^*(\omega) = G'(\omega)+iG''(\omega)$ [1, 2].

In the standard treatment of the experimental data, the fluid-dynamical problem is simplified too because, typically, expressions derived from simple analytical solutions of the Navier-Stokes equations [1], supplemented with the boundary conditions appropriate to the instrument geometry, are used to relate shear stress to shear rate or shear deformation [1, 2]).

In spite of these simplifications, the analysis of experimental bulk rheological data is often complicated by the presence of perturbations due to the flow or the instrument, such as instrument inertia ([7]), fluid inertia ([8, 9]), or both ([10, 11]). Hence, the proper analysis of rheological experimental data is still a subject of active research [12, 13, 14].

In the case of interfacial systems, further complications appear due to the presence of the fluid subphase and the unavoidable coupling of the velocity fields at the interface and the subphase, the different geometries that may be imposed at the interface (planar Langmuir troughs or spherical drop or bubble geometries), and the possibility of having simultaneously different types of deformation (shear, extensional, and dilatational). Several books [15, 16] and review articles [17, 18, 19, 20] have reviewed different aspects of interfacial rheology from both the experimental and theoretical points of view.

Regarding interfacial shear rheometers, a nice account and description of many of the instruments designed up to 2009 can be found in Krägel [21]. Since then other highly sensitive instruments have been proposed, namely, the double wall-ring (DWR) ISR [22], the microbutton ISR [23, 24, 25, 26], and the magnetic tweezers ISR using commercial [27] or microwire [28] probes.

Since the first attempts to design instruments capable of measuring mechanical properties of interfacial systems [29, 30] it became apparent that the role of the liquid subphase should be considered carefully [31, 32, 33]. In interfacial rheometry, the bulk fluid phases are typically assumed to be Newtonian, so that the Navier-Stokes equations with constant viscosity are used to represent the upper and lower fluid phases, while the interface is usually represented by the Boussinesq-Scriven boundary condition ([34, 15]) which represents the equilibrium of stresses tangential to the interface, and introduces the coupling between the bulk and interfacial velocity fields into the mathematical representation of the problem.

At an air/liquid interface, the relative importance of the interfacial and bulk stresses is represented by the Boussinesq number [22],

$$Bo^* = \frac{\eta_s^* \, P_s \, \frac{V}{L_s}}{\eta_b \, A_b \, \frac{V}{L_b}}, \tag{1}$$

where η_s^* is the complex interfacial viscosity, P_s is the perimeter of the contact line along the probe surface, η_b is the bulk phase viscosity, A_b is the contact area between the probe and the bulk phase, V is a characteristic velocity scale (e.g., the velocity at the probe rim), and L_s and L_b are characteristic length scales of velocity decay at the interface and bulk phases, respectively.

When the Boussinesq number is high (say $Bo^* > 100$), interfacial stresses dominate the system dynamics and the flow at the bulk phase is dominated by the interfacial flow. Conversely, when the Boussinesq number is small, the bulk flow dominates and the interfacial flow follows the flow at the bulk phase.

In any case, in order to achieve a proper characterization of the interfacial viscoelasticity of a given sample, a correct separation of interfacial and subphase effects in the system response is mandatory. Such separation requires the introduction of non-oversimplified physical models that include the coupling of the interfacial and bulk flow fields and that are suitable for implementation of fast numeric computational schemes.

Since the seminal work of Reynaert et al. [35], such schemes have been publicized for the most popular interfacial shear rheometer configurations, namely, the magnetic needle ISR (MNISR hereafter) in both the Helmholtz coils [35, 36, 28], and the magnetic tweezers [27] configurations, the double wall-ring (DWR) rotational interfacial shear rheometer [22], and the bicone bob rotational interfacial shear rheometer [37, 38, 39]. Fortunately, the availability of fast hardware (multi-kernel microprocessors and graphic cards) and fast computational platforms (MATLAB®, GNU Octave, Python®, *Mathematica*®, etc.) has shortened the time cost of the required computations so that nowadays the computational work can be performed nearly in real time during the experiments.

In this report we will review the most salient developments concerning the application of flow field-based data analysis techniques in the field of interfacial shear rheology. Our intention is to give a full account of the developments on the different geometries already published, particularly focusing on the technical aspects. Experimental data will be introduced to illustrate the benefit of flow field-based methods when applied to the analysis of bulk rheology data, being this application new, to our knowledge. For the experimental checks concerning the application of flow field-based data analysis to interfacial rheology data, the readers are referred to the bibliography purposely cited in each section. In Section 2 we will make a brief general overview of the common aspects of the flow field-based data analysis schemes developed in the last years, together with some comparative performance test against other data analysis approaches based on simple analytic flow field configurations. Section 3 will review the details of the different implementations of such techniques concerning the MNISR. Section 4 will address the application of such techniques to the DWR ISR, while Section 5 will focus on the bicone bob rotational ISR. Section 6 will sketch some new developments, namely the extension of the technique to the microbutton ISR and the application of such techniques to bulk rheometry of soft samples. Finally, in Section 7 we briefly compile some conclusive remarks and final comments.

2. Method overview

Experimental interfacial shear rheology (ISR) techniques generally use a probe that exerts a shear deformation on the interface. We refer to techniques in which an external force, $\boldsymbol{F}(t)$ (or torque $\boldsymbol{M}(t)$ when a torsion rheometer is used), is applied on the probe in a controlled manner as *active* ISR techniques. In this review we will confine ourselves to discuss the three most extended experimental setups mentioned in the Introduction; according to the characteristic length of their probes, we can refer to such devices as *macro-rheometers*. However, active *micro-rheometers* have also been designed, generally comprising microparticles trapped at the interface and optical or magnetic tweezers to apply a controlled $\boldsymbol{F}(t)$ on them. For details on the hydrodynamical models proposed for such *micro-rheometers*, the reader is addressed to Refs. [40, 41, 42, 43, 44, 45].

In the *macro-rheometers* analyzed in this review, the displacement of the probe, $\boldsymbol{l}_p(t)$ ($\theta_p(t)$ in rotational rheometers), is known through optical inspection (or through the rotor angular displacement when a torsion rheometer is used). The three experimental approaches essentially differ in the geometrical parameters of the sample under study, and the shape, size, and mass of the probe. In practice, all probes have a finite size so that, firstly, they are in contact with the interface and the adjacent bulk phases and, secondly, they have inertia. Hence, the motion of the probe is affected by several contributions, where the interfacial drag is just one of them. While, in a first approximation (considering the interfacial velocity profile as linear), the interfacial strain $\gamma_s(\boldsymbol{r}, t)$ can be easily calculated from $\boldsymbol{l}_p(t)$ (or $\theta_p(t)$), the non-trivial coupling of the above-mentioned contributions makes the problem much more complex when it comes to calculating the interfacial stress, $\sigma_s(\boldsymbol{r}, t)$, from $\boldsymbol{F}(t)$ or $\boldsymbol{M}(t)$ (we will use the subscript s to refer to interfacial parameters, while the corresponding symbols without subscript refer to the same magnitudes in the bulk phases).

The relative importance of the interfacial contribution with respect to the total force (or torque) on the probe (bulk phases contribution, probe inertia, and device contribution) determines whether the relation between $\boldsymbol{F}(t)$ or $\boldsymbol{M}(t)$ and $\sigma_s(\boldsymbol{r}, t)$ can be simplified, without a significant cost in the accuracy of the method, or whether more precise schemes, such as the explicit calculation of the flow field, are mandatory. The non-dimensional Boussinesq number, Bo, is the ratio of the interfacial drag to the bulk phases drags on the probe, and is in general a good estimator in this regard.

For the remainder of this review, we will focus on dynamical experiments where a one-dimensional oscillatory force (or torque) with angular frequency ω is imposed on the probe, which follows an oscillatory motion with the same frequency

$$
\begin{aligned}
F^*(t) = F_0 \exp\{i\omega t\} \Rightarrow l_p^*(t) = l_0 \ \exp\{i(\omega t + \delta_l)\} = l_0^* \ \exp\{i\omega t\}, \\
M^*(t) = M_0 \exp\{i\omega t\} \Rightarrow \theta_p^*(t) = \theta_0 \ \exp\{i(\omega t + \delta_\theta)\} = \theta_0^* \ \exp\{i\omega t\},
\end{aligned} \quad (2)
$$

where F_0 (M_0) is the amplitude of the force (torque) imposed, and l_0^* (θ_0^*) is the amplitude of the longitudinal (angular) displacement of the probe, being its imaginary part the out-of-phase component of such displacement with respect to the force (torque). The physical magnitudes defined in Eq. (2) are the experimental observables that are usually combined to define a single observable: the complex amplitude ratio, AR^*,

$$
\begin{aligned}
AR_l^* &= \frac{F_0}{l_0^*}, \\
AR_\theta^* &= \frac{M_0}{\theta_0^*}.
\end{aligned} \tag{3}
$$

If we assume that i) the motion of any fluid element is also oscillatory with the same frequency ω and with only one non null velocity component in an adequate reference frame, ii) the interfacial system under study and the bulk phases are homogeneous and isotropic, and iii) the interfacial system is flat and strictly two-dimensional, we can re-write the stress and strain in the surface and the bulk phases as

$$
\begin{aligned}
\sigma_s^*(\boldsymbol{r}, t) = \sigma_{s,0}^*(\boldsymbol{r}) \exp\{i\omega t\}, &\quad \sigma^{*(1,2)}(\boldsymbol{r}, t) = \sigma_0^{*(1,2)}(\boldsymbol{r}) \exp\{i\omega t\}, \\
\gamma_s^*(\boldsymbol{r}, t) = \gamma_{s,0}^*(\boldsymbol{r}) \exp\{i\omega t\}, &\quad \gamma^{*(1,2)}(\boldsymbol{r}, t) = \gamma_0^{*(1,2)}(\boldsymbol{r}) \exp\{i\omega t\},
\end{aligned} \tag{4}
$$

where the expressions on the left side correspond to the interface and the expressions on the right side correspond to the bulk phases, being the superscripts 1 and 2 the indication for the lower bulk phase, or subphase, and the upper bulk phase, respectively. The imaginary part of the strain and stress amplitudes in Eq. (4) arises from the phase lag with respect to the phase reference (the external force or torque). Note that, given the non-trivial coupling of all the contributions to the probe motion, there may be a phase difference between the external force (or torque) and the stress imposed on the interface and the bulk phases. Using the Kelvin-Voigt model and considering the oscillatory problem, stress and strain are related by

$$
\begin{aligned}
\frac{\sigma_s^*(\boldsymbol{r}, t)}{\gamma_s^*(\boldsymbol{r}, t)} &= \frac{\sigma_{s,0}^*(\boldsymbol{r})}{\gamma_{s,0}^*(\boldsymbol{r})} = G_s^* = G_s' + iG_s'', \\
\frac{\sigma^{*(1,2)}(\boldsymbol{r}, t)}{\gamma^{*(1,2)}(\boldsymbol{r}, t)} &= \frac{\sigma_0^{*(1,2)}(\boldsymbol{r})}{\gamma_0^{*(1,2)}(\boldsymbol{r})} = G^{*(1,2)} = G'^{(1,2)} + iG''^{(1,2)}.
\end{aligned} \tag{5}
$$

Analogously, a complex viscosity is defined as

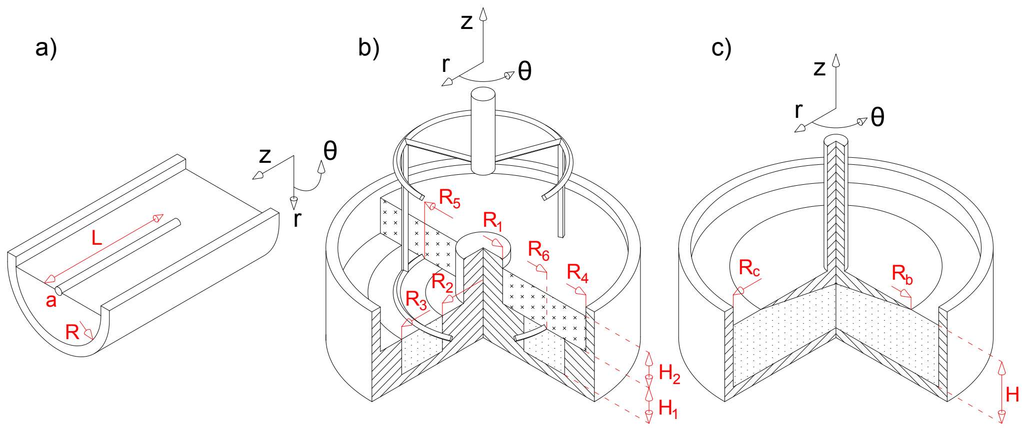

Figure 1: Schematics of the three interfacial rheometers discussed in this review, along with the corresponding frame of reference. a) Magnetic needle interfacial stress rheometer, where a is the radius of the needle, L is its length, and the shear channel is cylindrical with radius R. b) Double wall ring, where R_1 and R_4 are the inner and outer radius of the cup containing the upper phase, respectively. R_2 and R_3 are the inner and outer radius of the cup containing the subphase, respectively. The ring has a rhomboidal cross section and is placed with its two co-planar edges pinned to the interface. The inner and outer radius of the ring are R_5 and R_6, respectively. H_1 is the height of the fluid sub-phase, and H_2 is the height of the upper phase. c) Bicone setup, where R_b is the radius of the bicone fixture, and R_c is the radius of the cup containing the sample. H is the height of the fluid sub-phase.

$$\begin{aligned} \eta_s^*(\omega) &= \frac{G_s^*}{i\omega} = \frac{G_s''}{\omega} - i\frac{G_s'}{\omega} = \eta_s'(\omega) - i\eta_s''(\omega), \\ \eta^{*(1,2)}(\omega) &= \frac{G^{*(1,2)}}{i\omega} = \frac{G''^{(1,2)}}{\omega} - i\frac{G'^{(1,2)}}{\omega} = \eta'^{(1,2)}(\omega) - i\eta''^{(1,2)}(\omega), \end{aligned} \tag{6}$$

which is related to the stress and strain by

$$\begin{aligned} \eta_s^*(\omega) &= \frac{\sigma_s^*(\boldsymbol{r},t)}{\dot{\gamma}_s^*(\boldsymbol{r},t)} = \frac{\sigma_s^*(\boldsymbol{r},t)}{i\omega\gamma_s^*(\boldsymbol{r},t)}, \\ \eta^{*(1,2)}(\omega) &= \frac{\sigma_s^{*(1,2)}(\boldsymbol{r},t)}{\dot{\gamma}_s^{*(1,2)}(\boldsymbol{r},t)} = \frac{\sigma_s^{*(1,2)}(\boldsymbol{r},t)}{i\omega\gamma_s^{*(1,2)}(\boldsymbol{r},t)}, \end{aligned} \tag{7}$$

where the dot indicates a time derivative.

The goal of any hydrodynamical model applied to interfacial rheology is writing down Eq. (5) as a function of known observables, i.e. the geometrical parameters of the setup and the experimentally measured amplitude ratio AR^*. Consequently, the way in which Eq. (5) is implemented in each model defines the corresponding data analysis scheme. Before describing the most relevant hydrodynamical models, let us introduce the three experimental approaches discussed in this paper. They will be thoroughly described in the following section, so that, at this point, we will just describe their key aspects in order to have an adequate context for the hydrodynamical models. The schematics of the experimental setups are presented in Fig. 1. In the MNISR (Fig. 1a), the probe consists of a magnetic needle resting on the interface along the center of a shear channel. An external magnetic force is exerted on the needle in such a way that it describes an oscillatory displacement along the axis of the channel, $\boldsymbol{l}_p(t) = z_0^* \exp\{i\omega t\}$. Thus, the amplitude ratio is in this case $AR_l^* = F_0/z_0^*$. In the double-wall-ring (DWR) setup (Fig. 1b), a thin ring is attached to the rotor of a torsion rheometer. The rotor is vertically displaced until the ring rests at the interface in between two coaxial cylindrical walls that form the shear channel. In this setup, the observable is $AR_\theta^* = M_0/\theta_0^*$, where M_0 is the amplitude of the torque imposed by the rotor and θ_0^* is the angular displacement of the rotor. The conical bob setup (Fig. 1c) also consists of a torsion rheometer in which a conical shaped fixture is attached. In this case, the shear channel is formed between the conical bob rim and the lateral wall of the cup containing the sample, and the experimental observable takes the same form as for the DWR setup.

2.1. Simple models: linear velocity profile and simply additive contributions

The simplest model one can come up with consists of making two assumptions: first, the interfacial drag is the only relevant contribution to the probe dynamics; thus, the external force on the probe is entirely applied to the interface along the contact line between the probe and the interface. The second assumption considers that the velocity profile at the interface is linear. To be more precise, one can consider that the interface and the bulk phases are decoupled assuming that $|Bo^*| \to \infty$ and calculating the corresponding shear strain at the interface. From this assumption, the velocity profile at the interface for the MNISR is simply linear, so that the strain is constant through the shear channel (see the expression for $\sigma_{s,0}^*$ in the Table 1). In the DWR and the bicone, imposing $|Bo^*| \to \infty$ in the momentum balance equation at the interface (the particular form of this equation will be discussed in detail in Secs. 4 and 5) yields the expressions for $\gamma^*_{s,0}$ at the probe contact line that we summarize in Table 1. The corresponding expressions for G^*_s for this model are summarized in the second-to-last column of Table 1.

Under some experimental circumstances, one can take a step forward in the accuracy of the model by accounting for the rest of the contributions in a simple manner. Assuming that all the contributions to the probe dynamics are simply additive (the interfacial drag plus the additional contributions, i.e. bulk phases drag, probe's inertia, other eventual device contributions), and that the additional contributions are independent of the interface drag, one would be able to subtract the additional contributions from the experimental raw data as long as such additional contributions are known. This knowledge can be obtained by performing a *calibration* experiment, which must be performed in the same condition as the *real* experiment (same probe, frequency, and bulk phases) but in the absence of the interfacial system under study, i.e., with a *clean* air/subphase interface. The amplitude ratio measured in these conditions, which we will refer to as AR^*_{cal}, can be subtracted from the experimental amplitude ratio with the interfacial system in place, AR^*_{exp}, so that the *effective* amplitude ratio is $AR^*_{eff} = AR^*_{exp} - AR^*_{cal}$. The expressions for this model are summarized in the last column of Table 1.

These two models (linear approximation with and without calibration experiment, respectively) have the benefit of a very simple data analysis scheme, since the calculation of G^*_s from the experimental AR^* is immediate with no computational cost. However, it is clear that the aforementioned approximations are valid only when the interfacial drag is much larger than the rest of the contributions. Moreover, while the subtraction of the additional contributions enhances the accuracy of the model, the assumption of such contributions as simply additive and independent of the interfacial drag is not necessarily valid. And more importantly, the strain does not follow, in general, the expressions in Table 1 because, for $Bo \sim 1$, the coupling with the bulk phases makes the velocity profile at the interface decay in the vicinity of the probe in motion.

An enlightening discussion on the characteristic length scales for both interfacial and bulk flows in the MNISR can be found in Ref. [46], where the authors define the viscous length scales at both the bulk subphase, ℓ_ω, and at the interface, ℓ^s_ω, as

	Linear approximation				Calib. subtraction
	AR^*_{exp}	$\sigma^*_{s,0}$	$\gamma^*_{s,0}$	G^*_s	G^*_s
ine MNISR	$\frac{F_0}{z^*_0}$	$\frac{F_0}{2L}$	$\frac{z^*_0}{R-a}$	$\frac{AR^*_{exp}(R-a)}{2L}$	$\frac{(AR^*_{exp}-AR^*_{cal})(R-a)}{2L}$
Bicone	$\frac{M_0}{\theta^*_0}$	$\frac{M_0}{2\pi R_b^2}$	$\frac{\theta^*_0 2R_c^2}{R_c^2-R_b^2}$	$\frac{AR^*_{exp}(R_c^2-R_b^2)}{4\pi R_b^2 R_c^2}$	$\frac{(AR^*_{exp}-AR^*_{cal})(R_c^2-R_b^2)}{4\pi R_b^2 R_c^2}$
DWR$^{\mathrm{i}}$		$\frac{M_1}{2\pi R_5^2}$	$\frac{\theta^*_0 2R_1^2}{R_5^2-R_1^2}$		
DWR$^{\mathrm{ii}}$		$\frac{M_2}{2\pi R_6^2}$	$\frac{\theta^*_0 2R_3^2}{R_3^2-R_6^2}$		
DWR$^{\mathrm{iii}}$	$\frac{M_0}{\theta^*_0}$			$\frac{AR^*_{exp}}{4\pi\left(\frac{R_5^2R_1^2}{R_5^2-R_1^2}+\frac{R_6^2R_3^2}{R_3^2-R_6^2}\right)}$	$\frac{AR^*_{exp}-AR^*_{cal}}{4\pi\left(\frac{R_5^2R_1^2}{R_5^2-R_1^2}+\frac{R_6^2R_3^2}{R_3^2-R_6^2}\right)}$

Table 1: Summary of the expressions corresponding to the amplitude ratio, surface stress, surface strain and complex interfacial modulus, G^*_s, in the linear approximation for the three geometries analyzed in the present review (MNISR, bicone, and DWR). The right column shows the expressions for G^*_s introducing the subtraction of the additional contributions, AR^*_{cal}. The row DWR$^{\mathrm{i}}$ shows the surface stress and strain at the inner contact line of the ring (R_5). In this row, M_1 is the part of the total torque applied to the inner interface. The row DWR$^{\mathrm{ii}}$ shows the surface stress and strain at the outer contact line (R_6), being M_2 the torque applied to the outer interface. The row DWR$^{\mathrm{iii}}$ shows the resulting expression for G^*_s, where $M_0 = M_1 + M_2$.

$$\ell_\omega = \sqrt{\frac{\nu}{\omega}},$$
$$\ell^s_\omega = \sqrt{\ell_\omega \frac{\eta^*_s}{\eta}}, \tag{8}$$

where ν is the kinematic viscosity of the bulk subphase ($\nu = \eta/\rho$, being ρ the density). ℓ_ω and ℓ^s_ω represent the distance at which momentum decays at the bulk subphase and at the interface, respectively. In practice, the size of the bulk phase in the direction perpendicular to the interface (the depth of the bulk phase) is typically much larger than ℓ_ω, so that the relevant length scale in the bulk phase is ℓ_ω. However, the width of the shear channel may be smaller or larger than ℓ^s_ω depending on the value of η^*_s. The analysis for the MNISR and the bicone geometries depicted in Refs. [46, 37] shows that these interfacial rheometers are sensitive to values of η^*_s small enough to verify $\ell^s_\omega < (R-a)$ (or $\ell^s_\omega < (R_c - R_b)$). In such cases, the interfacial velocity profile decreases exponentially within a distance ℓ^s_ω from the probe in motion, so that the actual surface strain deviates from those written in

Table 1. Thus, the simple models described above, and summarized in Table 1, overestimate the value of G_s^* calculated from the experimental AR^*. The overestimation can be of several orders of magnitude at low values of Bo, and safely negligible at high values of Bo. We will quantify the overestimation of the simple models as a function of G_s^* at the end of this section.

2.2. Flow field-based models

The eventual non-linear velocity profile at the interface, and the proper separation of all the contributions to the probe dynamics, can be solved by means of the explicit calculation of the flow field at the interface and the bulk phases. Assuming that all the fluid elements describe an oscillatory motion in which there is only one non null velocity component (as that of the probe), we can define an amplitude function $g^*(\boldsymbol{r})$ that relates the velocity of the fluid element located at $\boldsymbol{r}$ to the velocity of the probe

$$v(\boldsymbol{r}, t) = g^*(\boldsymbol{r}) v_p(t), \tag{9}$$

being $v_p(t)$ the velocity of the probe. The imaginary part of $g^*(\boldsymbol{r})$ stands for the out-of-phase component of the fluid element velocity with respect to the probe velocity. With the appropriate boundary conditions, one can write down, and numerically solve, the Navier-Stokes equations, finding the solution for the amplitude function $g^*(\boldsymbol{r})$ for the volume occupied by the shear channel (including both bulk phases). Once the flow field is known, the separation of the bulk and interface contributions to the probe dynamics is achieved through the integration of the gradients of g^* over the corresponding contact areas (contact line in the case of the interface). Analytically, the contribution of the surface and bulk phases drags to the amplitude ratio takes the form

$$\begin{aligned}
AR^*_{surf} &= G_s^* \int_L (\nabla g^*(\boldsymbol{r})) \cdot \boldsymbol{s}\, dL, \\
AR^*_{bulk} &= G^{*(1)} \left[\int \int_{S_1} (\nabla g^*(\boldsymbol{r})) \cdot \boldsymbol{n}_1\, dS \right] + G^{*(2)} \left[\int \int_{S_2} (\nabla g^*(\boldsymbol{r})) \cdot \boldsymbol{n}_2\, dS \right],
\end{aligned} \tag{10}$$

where $\boldsymbol{s}$ is the unitary vector tangent to the interface and perpendicular to the probe-interface contact line, and $\boldsymbol{n}_1$ and $\boldsymbol{n}_2$ are the unitary vectors perpendicular to the contact area between the probe and the bulk phases 1 and 2, respectively. L represents the contact line between the probe and the interface, and S_1 and S_2 stand for the contact surfaces between the probe and bulk phases 1 and 2, respectively.

The force balance equation can now be outlined, which will contain terms for the probe inertia and any other possible device contribution

$$AR^*_{exp} - AR^*_{surf} - AR^*_{bulk} + AR^*_{dev} = AR^*_{inertia}, \tag{11}$$

where AR^*_{dev} represents all the additional contributions from the device (centering potential in the MNISR, bearing friction, etc...), and $AR^*_{inertia}$ stands for the probe inertia, which is known as long as its mass (or moment of inertia) is known.

The term AR^*_{dev} may have different origin depending on the interfacial rheometer geometry. For instance, in the rotational rheometer configurations (DWR or bicone) residual friction in the air bearing represents the major contribution to AR^*_{dev}, although its effect is very minor. Conversely, in magnetic needle ISRs, static trapping subsystems, typically used to avoid the probe scaping from the measurement window, usually introduce a constant contribution to AR^*_{dev} [28, 27] that strongly limit the instrument resolution at low oscillation frequency.

Eq. (11) relates the experimental observable, AR^*_{exp}, to the interfacial dynamic moduli, G^*_s, via AR^*_{surf}. However, once the experiment is executed and AR^*_{exp} is known, Eq. (11) does not allow for the direct calculation of G^*_s because the drag terms depend on $g^*(\boldsymbol{r})$ (the flow field), which, in turn, depends on G^*_s. Thus, an iterative procedure is needed to find the proper value of G^*_s that matches the experimentally obtained AR^*_{exp}.

The algorithm that allows for the calculation G^*_s from the experimental observable has the same structure for the three geometries here studied (indeed, it does not depend on the geometry, so it can be applied to any other device as long as the flow field can be obtained). First, one has to define the simplest flow configuration consistent with the specific geometry, where any fluid element follows the motion of the probe as $v(\boldsymbol{r}, t) = g^*(\boldsymbol{r})v_p(t)$. Second, assuming the no-slip condition at the shear channel walls and the probe surface, and the Boussinesq-Scriven condition at the interface, the Navier-Stokes equations are solved, obtaining the amplitude function $g^*(\boldsymbol{r})$. Third, the interface and bulk drag contributions are calculated from $g^*(\boldsymbol{r})$, which allows one to write the force, or torque, balance equation with all the contributions to the probe dynamics explicitly separated. Fourth, an iterative scheme must be built to find the value of η_s^* that provides the best fit to the experimental observable, AR_{exp}.

In the next sections, we will discuss in detail the physical model, the mathematical formulation, and the numerical scheme needed to find the complex velocity amplitude function $g^*(\boldsymbol{r})$ for the three geometries analyzed, along with the particular form of the Eq. (11) and the iterative procedure to find G_s^*.

2.3. Comparative performance tests.

We will conclude this section with a numerical comparison of the performance of the three models here described (linear approximation, with and without calibration experiment, and flow field-based) through the results of their corresponding data analysis schemes for the MNISR and the bicone geometries. For that purpose we have fed the three data analysis schemes with the values of AR^*_{exp}, obtained by solving the full hydrodynamic and probe motion problem for an air/water interface with an interfacial film of given complex interfacial viscosity η_s^*, and AR^*_{cal}, obtained by solving the full hydrodynamic and probe motion problem for a clean air/water interface ($Bo^* = 0$).

Three cases of interfacial films with different rheological behavior have been considered: i) purely viscous interfaces ($\eta_s^* = \eta_s' = \eta_s$) at a moderately high frequency ($\omega = 10\pi$ rad/s), ii) viscoelastic interfaces ($\eta_s^* = \eta_s' - i\eta_s'' = \eta_s(1-i)$) at an intermediate frequency ($\omega = \pi$ rad/s), and iii) purely elastic interfaces ($\eta_s^* = -i\eta_s'' = -i\eta_s$) at a low frequency ($\omega = \pi/10$ rad/s). The values of η_s span the range 10^{-7} Ns/m $\leq \eta_s \leq 10$ Ns/m. The numerically obtained values of AR^*_{exp} and AR^*_{cal} are substituted into the expressions in the central and right columns of Table 1, for the two linear approximation models, and into the version of Equation (11) corresponding to each geometry for the flow field-based analysis. The values of η_s^* obtained through each of the three data analysis schemes for each geometry, which we will refer to as the apparent surface viscosity $\eta^*_{s,app}$, are then compared with the original ones that were used to obtain the full flow field configuration and, consequently, the complex amplitude ratio values fed to the data analysis schemes. Therefore, the overestimation introduced by the oversimplification implicit in the linear approximation models can be quantified.

The results are summarized in Figure 2, where the top, middle, and bottom rows correspond, respectively, to the purely viscous, viscoelastic, and purely elastic interfaces. The panels at left and right columns show, respectively, the ratio between the moduli and the difference between the arguments of the apparent (calculated) and original values of η_s. The lines with circles, triangles, and squares belong to the simple linear approximation, the linear approximation with calibration subtraction, and the flow field-based data analysis, respectively. Blue graphs correspond to the MNISR and magenta graphs to the bicone geometry.

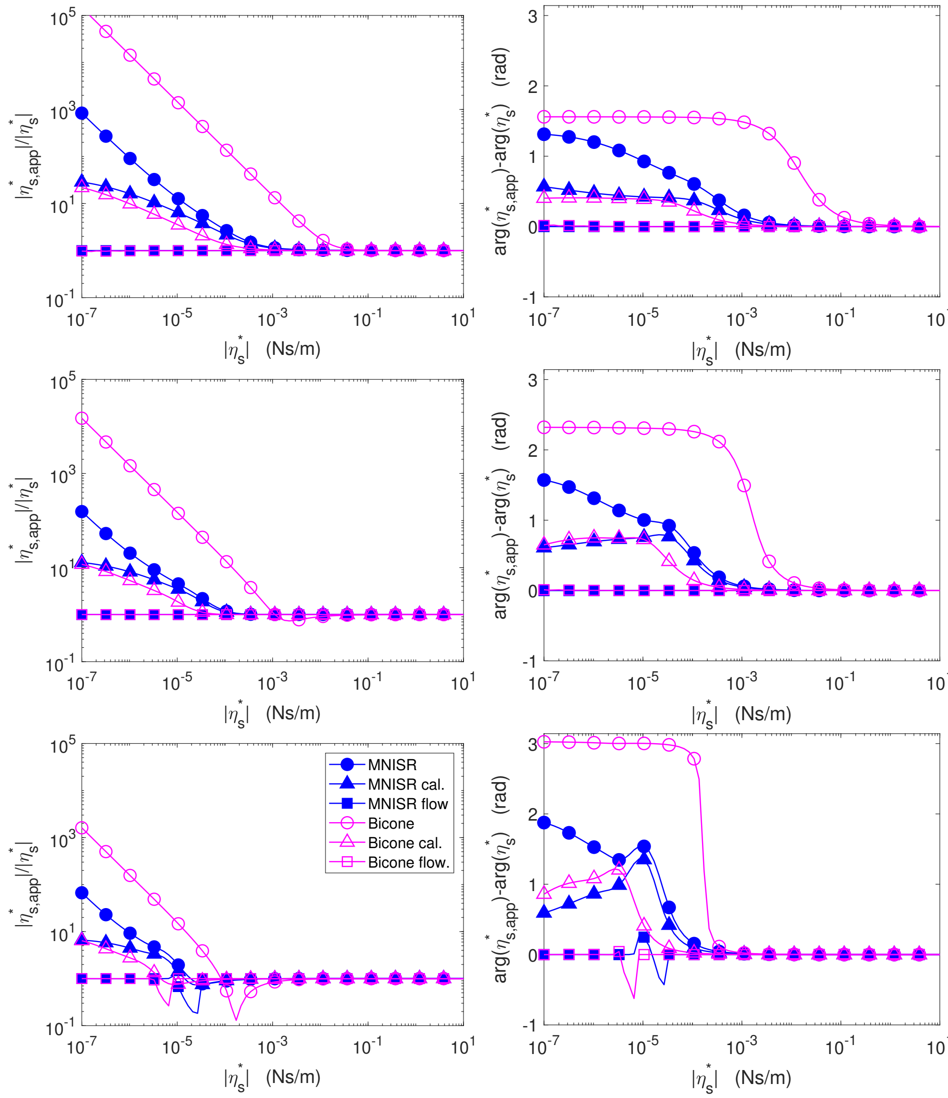

Figure 2: Comparative performance test on purely viscous interfaces ($\eta_s^* = \eta_s$) at $\omega = 10\pi$ rad/s (top row panels), viscoelastic interfaces ($\eta_s^* = \eta_s - i\eta_s$) at $\omega = \pi$ rad/s (central row panels), and purely elastic interfaces ($\eta_s^* = -i\eta_s$) at $\omega = \pi/10$ rad/s (lower row panels). Left panels: ratio of the moduli of the calculated and initial interfacial viscosities; right panels: difference between the arguments of the calculated and initial interfacial viscosities. The curves with circles, triangles, and squares correspond to the linear approximation, the linear approximation with calibration subtraction, and the flow field based model, respectively. The legend in the bottom left panel applies to all the graphs in this figure.

As can be seen in Figure 2, all of the three schemes yield correct results above a certain crossover value of η_s^* which depends on the data analysis scheme. The simplest linear approximation for the bicone case has the highest crossover value, most probably due to the high subphase drag torque of such configuration. On the other hand, the flow field-based data analysis schemes yield extremely good results all over the range of interfacial viscosity here studied, indicating that the iterative procedure is capable of finding the initial value of η_s^*. Two remarks are in order here. First, the case of the purely elastic interface shows qualitatively analogous results although it yields at some points underestimated values of the interfacial elasticity, most probably due to resonance phenomena [39]. Second, the analysis here outlined does not take into account the experimental uncertainty which is different for the different geometries [27, 38, 47].

In any case, the comparison here outlined shows that both versions of the linear approximation model display cross-over values of the interfacial viscosity below which using a flow field-based model and data analysis scheme is mandatory in order to have an accurate translation of the experimental raw data into values of the rheological parameters.

3. The magnetic needle interfacial stress rheometer

First introduced by Shahin [48] and later developed by Brooks et al. [49], the MNISR has been extensively used to explore the mechanical response of fluid-fluid interfaces. A number of research groups have used this setup to study the mechanical response of particle-laden interfaces [50], lipid Langmuir monolayers [51], such as lung surfactant [52, 53], contact lens tear films [54], or fatty acids/alcohols [55], and protein adsorbed (Gibbs) monolayers [56].

The classical design of the MNISR comprises a pair of Helmholtz coils through which an electrical current is driven in such a configuration that a potential well is established and the equilibrium position (and orientation) of the needle is fixed at the center of the shear channel (see Fig. 1a). The application of an oscillatory current through a second pair of coils (or its superposition in the first pair of coils) imposes an oscillatory force on the needle. Then, the needle exerts a stress and, by means of its longitudinal displacement, a strain on the interface (and the adjacent bulk phases). For more details on the setup design, the reader is addressed to Refs. [49, 35, 36, 28].

Brooks et al. [49] demonstrated that, with the needle placed on a clean air-water interface, the system is well described by a driven damped oscillator, where the elastic contribution is due to the centering potential and the damping is a consequence of the water subphase drag

$$\frac{F_0}{z_0^*} = k - m\omega^2 + i\omega d, \tag{12}$$

where m is the needle mass, k is the elastic constant of the centering potential, and d is the damping coefficient (water subphase drag).

The experimental observables are the electrical current flowing through the coils and the needle displacement. In order to obtain the experimental amplitude ratio, $AR^*_{exp} = F_0/z_0^*$, it is necessary to convert the electrical current into magnetic force on the needle. This can be achieved by means of a frequency sweep at high frequencies, where the probe inertia dominates. Since the mass of the needle is known, the proportionality constant between electrical current and force, which we will refer to as C, can be obtained. The other unknown parameter of the device, the elastic constant of the centering potential, k, can be obtained by means of a frequency sweep at low frequencies, where the frequency dependent terms become negligible and the only relevant term is k. Once the device is calibrated on a clean air-water interface, AR^*_{cal} is known and the experiments with the interfacial system in place can be performed.

The procedure to obtain the flow field in the shear channel of the MNISR was proposed by Reynaert et al. [35], where they described, first, the numerical scheme to calculate the amplitude function $g^*(\boldsymbol{r})$ and, second, the particular form of Eq. (11) for this device. Regarding the solution of the Navier-Stokes equation, consider the geometry described in Fig. 1a, where the shear channel is cylindrical with radius R, being a the rod radius, and one bulk phase with viscosity η. Assuming that all the fluid elements move with a single non null velocity component (along the z axis in this case), the Navier-Stokes equation takes the form

$$\eta \nabla^2 \frac{\partial z(\boldsymbol{r}, t)}{\partial t} = \rho \frac{\partial^2 z(\boldsymbol{r}, t)}{\partial t^2}, \tag{13}$$

where ρ is the bulk fluid density and $z(\boldsymbol{r}, t)$ is the fluid displacement. Using the cylindrical coordinate system indicated in Fig. 1a and the substitution

$p = \log(r/a)$, the Navier-Stokes equation in terms of the amplitude function $g^*(p, \theta)$ takes the form

$$\frac{\partial^2 g^*(p,\theta)}{\partial p^2} + \frac{\partial^2 g^*(p,\theta)}{\partial \theta^2} = i\, Re\, g^*(p,\theta) e^{2p}, \tag{14}$$

where Re is the Reynolds number defined as

$$Re = \frac{\rho a^2 \omega}{\eta}. \tag{15}$$

The boundary conditions are no-slip at the needle and channel walls, and the mechanical response of the interface is introduced via the Boussinesq-Scriven boundary condition at the interface, which for this geometry takes the form

$$Bo^*\, e^{-p} \left(\frac{\partial^2 g^*(p,\theta)}{\partial p^2} - \frac{\partial g^*(p,\theta)}{\partial p} \right) - \frac{\partial g^*(p,\theta)}{\partial \theta} = 0, \quad \text{at } \theta = \pi/2, \tag{16}$$

where the Boussinesq number is defined as

$$Bo^* = \frac{\eta_s^*}{a\eta}. \tag{17}$$

Eqs. (14)-(17) can be solved numerically by means of a centered finite differences scheme.

In Figure 3 we show color coded plots of the real and imaginary parts of the velocity amplitude function, $\Re[g^*(r, z)]$ (left panel), and $\Im[g^*(r, z)]$ (right panel), respectively. Calculations were made for a typical commercial magnetic needle ($a = 200\,\mu$m, $L = 30\,$mm, and $m = 1.30 \times 10^{-5}\,$kg) centered in a cylindrical channel having $R = 10\,$mm. The flow field has been calculated for $Bo^* = 50(1 - i)$ at a frequency $\omega = \pi$ rad/s, in a 300×300 mesh in the (p, θ) domain. Strong velocity gradients can be appreciated in the subphase close to the needle surface and at the interface.

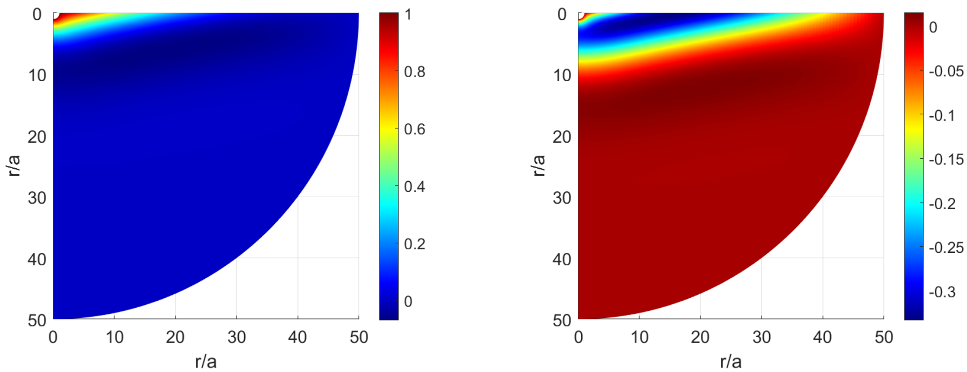

Figure 3: Color coded plots of (a) $\Re[g^*(r,\theta)]$, and (b) $\Im[g^*(r,\theta)]$ at $Bo^* = 50(1-i)$ and $\omega = \pi$ rad/s. The needle and shear channel radius are $a = 200\,\mu$m and $R = 10\,$mm, respectively.

Once the amplitude function $g^*(p,\theta)$ is known, it is particularly illustrative to analyze the shape of its profile at the interface $g_s^*(p) = g^*(p,\pi/2)$ or $g_s^*(r) = g^*(r,\pi/2)$, in (r,θ) coordinates. Figure 4 shows the interfacial velocity profile for three cases of viscoelastic interfaces with complex viscosity values ranging from $\eta_s^* = 10^{-7}(1-i)\,$Ns/m to $|\eta_s^*| \to \infty$ and at a frequency $\omega = \pi$ rad/s. Solid and dashed lines represent, respectively, the real, $\Re[g_s^*(r)]$, and imaginary, $\Im[g_s^*(r)]$, parts of the interfacial velocity profile.

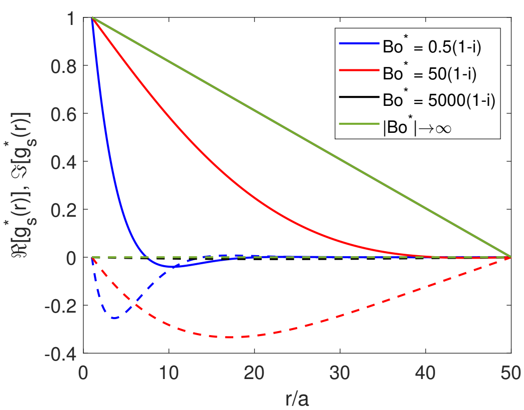

Figure 4: Real and imaginary parts of $g_s^*(r)$ for viscoelastic interfaces at different Bo^* values for a magnetic needle probe with radius $a = 200\,\mu$m and a shear channel with radius $R = 10\,$mm. The surface viscosity values used in the calculations are: $\eta_s^* = 10^{-7}(1-i)\,$Ns/m (blue line); $\eta_s^* = 10^{-5}(1-i)\,$Ns/m (red line); $\eta_s^* = 10^{-3}(1-i)\,$Ns/m (black line); $\eta_s^* \to \infty$ (green line). All cases are calculated at $\omega = \pi$ rad/s. Continuous lines: $\Re[g_s^*(r)]$; dashed lines: $\Im[g_s^*(r)]$.

The analytical solution for the interfacial radial velocity profile corresponding to $|\eta_s^*| \to \infty$ or, equivalently, $|Bo^*| \to \infty$, has been obtained by considering an interface fully decoupled from the subphase, i.e., neglecting the bulk contribution to the interfacial shear stress balance (the gradient in the angular variable at equation (16)). The analytical solution reads $g_s(r) = \frac{R-r}{R-a}$, i.e., it is a strictly real function that describes a linear velocity profile in phase with the probe velocity (green line in Figure 4). As can be seen in the Fig. 4, it superimposes on the numerically calculated interfacial velocity profile for the high Bo^* case (black solid line).

Now it becomes clear why the linear approximation (assuming the surface shear strain as constant through the shear channel) fails at low η_s^*, demonstrating one of the reasons of the overestimation of G_s^* when ignoring the actual flow field calculation and using the simplest models instead (see last two columns in Table 1). Moreover, the out-of-phase component of the fluid velocity (dashed lines in Figure 4) becomes non-zero for low values of η_s^*, demonstrating that, first, as mentioned in Section 2, $\gamma_{s,0}^*$ may have a non-zero imaginary part, and second, that the simplest models not only overestimate the value of η_s^*, but also err in calculating the loss tangent (the ratio of the loss to the elastic surface modulus), as can be seen in Figure 2.

The particular form of the force balance equation (Eq. (11)) for the MNISR is [35]

$$\frac{F_0}{z_0^*} = AR_{exp}^* = -i2L\omega\eta Bo^* \left.\left(\frac{\partial g^*}{\partial p}\right)\right|_{p=0,\theta=\pi/2}$$
$$-i2L\omega\eta\int_0^{\pi/2}\left.\left(\frac{\partial g^*}{\partial p}\right)\right|_{p=0} d\theta + k - m\omega^2. \tag{18}$$

From left to right, the terms on the right hand side of this equation are AR_{surf}^*, AR_{bulk}^*, AR_{dev}^*, and $AR_{inertia}$. Notice that, in this design of the MNISR, $AR_{dev}^* \neq 0$, so that, besides the bulk drag and the inertia, there is an additional contribution from the device.

Later, Verwijlen et al. [36] used particles trapped at the interface to track the velocity profile, finding a very good agreement with the numerical solution of Eqs. (14)-(17). Moreover, they proposed an iterative scheme to calculate G_s^* from the experimentally measured AR_{exp}^* through Eq. (18); namely, they proposed a method to explicitly account for the flow field when analyzing experimental data. Initially, a first guess for Bo^* is used to solve Eqs. (14)-(17), which provides a numerically calculated value of the amplitude ratio F_0/z_0^*, which we will refer to as AR_{num}^*. Then, AR_{num}^* is compared to the experimentally measured AR_{exp}^*, obtaining the value of Bo^* for the next iteration as

$$[Bo^*]_{k+1} = \frac{AR_{num}^*}{AR_{exp}^*}[Bo^*]_k. \tag{19}$$

More recently, Tajuelo et al. [28] used thin magnetic microwires as a probe for the MNISR. These microwires are more than one order of magnitude smaller in diameter than the conventional needles, being their length similar, so that the bulk and inertia contributions are significantly diminished while the interfacial contribution remains essentially the same. Hence, the sensitivity of the rheometer is increased at low values of η_s^*. They also showed that the driven damped oscillator approximation for the calibration procedure (Eq. (12)) fails for the thin microwires because, due to its lower mass, the out-of-phase component of the subphase drag is not negligible. Thus, the explicit calculation of the flow field must also be considered for the device calibration (calculation of C and k). Tajuelo et al. [28] proposed a calibration procedure, later used in Ref. [47], that consists on defining a function $S(C,k)$ that represents, at each point, the sum of the squared differences between the Eq. (18) using the corresponding value of k, and the experimentally measured $AR^*_{cal}(\omega)$ in the proper units of N/m by means of the corresponding value of C. Then, the coordinates (C,k) that minimize the function S are selected as the calibration parameters.

In recent years, a new driving mechanism has been proposed for the MNISR [27], where the magnetic coils are replaced by a mobile magnetic trap consisting of two small permanent magnets. The magnetic trap is displaced in an oscillatory manner along the direction of the shear channel, and, as a consequence of the magnetic force on the needle, it is also displaced in the same direction with the same frequency, describing essentially the same motion as with the magnetic coils. The authors demonstrated [27] that the dynamics of this system is well represented by an elastic potential with constant k_{mt} whose equilibrium point describes an oscillatory motion along the axis of the shear channel.

The raw data in the mobile magnetic trap MNISR are the displacement of the magnetic trap, $z_{mt}(t) = z_{mt,0}\exp\{i\omega t\}$, and the displacement of the needle, $z_p(t) = z_0^*\exp\{i\omega t\}$. The amplitude ratio obtained through the force balance equation in terms of these observables is

$$\frac{z_{mt,0}}{z_0^*} = 1 + \frac{-i2L\omega\eta Bo^* \left.\left(\frac{\partial g^*}{\partial p}\right)\right|_{p=0,\theta=\pi/2} - i2L\omega\eta\int_0^{\pi/2}\left.\left(\frac{\partial g^*}{\partial p}\right)\right|_{p=0} d\theta - m\omega^2}{k_{mt}}, \tag{20}$$

which, for reasons that will be apparent soon, we will label as a position-position amplitude ratio, $[AR^*_{exp}]^{pp} = \frac{z_{mt,0}}{z_0^*}$, at variance with respect to the force-position amplitude ratio defined in (18). Indeed, the force-position amplitude ratio for the magnetic trap driving mechanism can be found by taking into account the fact that the magnetic force on the needle, F_0, can be calculated from z_{mt} and z_0^* as

$$F_0(t) = -k_{mt}\left(z_p(t) - z_{mt}(t)\right) = -k_{mt}\left(z_0^* - z_{mt,0}\right)e^{i\omega t}, \tag{21}$$

where k_{mt} is the spring constant belonging to the magnetic trap, which can be found by means of calibration experiments [27]. Hence, Eqs. (20) and (21) lead to

$$\frac{F_0}{z_0^*} = AR^*_{exp} = -i2L\omega\eta Bo^* \left.\left(\frac{\partial g^*}{\partial p}\right)\right|_{p=0,\theta=\pi/2}$$
$$-i2L\omega\eta \int_0^{\pi/2} \left.\left(\frac{\partial g^*}{\partial p}\right)\right|_{p=0} d\theta - m\omega^2. \quad (22)$$

The comparison of Eqs. (22) and (18) is illustrative: they are equivalent if $k = 0$ in Eq. (22). In other words, using a mobile magnetic trap as a driving mechanism keeps the probe dynamics essentially the same, but removes the device contribution ($AR^*_{dev} = 0$), increasing the relative importance of AR^*_{surf} with respect to the rest of the terms, which manifests as an increased sensitivity particularly at low frequency.

A variation of the iterative procedure indicated in Eq. (19) can be devised by solving for Bo^* in the expressions (18) or (22). For the case of the MTISR, following Eq. (22), it yields:

$$[Bo^*]_{k+1} = \frac{\left([AR^*_{exp}]^{pp} - 1\right) k_{mt} - i2L\omega\eta \int_0^{\pi/2} \left.\left(\frac{\partial [g^*]_k}{\partial p}\right)\right|_{p=0} d\theta + m\omega^2}{i2L\omega\eta \left.\left(\frac{\partial [g^*]_k}{\partial p}\right)\right|_{p=0,\theta=\pi/2}}, \quad (23)$$

where $[AR^*_{exp}]^{pp} = \frac{z_{mt,0}}{z_0^*}$.

Starting from an appropriate seed, the scheme is iterated till convergence. A suitable convergence criterion might be:

$$\left| \frac{[AR^*_{calc}]^{pp}_k - [AR^*_{exp}]^{pp}}{[AR^*_{exp}]^{pp}} \right| \leq tolMin, \quad (24)$$

where $[AR^*_{calc}]^{pp}_k$ is calculated following expression (20) in each step.

An important aspect in the evaluation of the procedure's performance is the capability of giving the correct Bo^* values in cases where the value of Bo^* is known. Such tests have been labeled as consistency tests [39] and can be easily done by feeding the data analysis scheme with values of the amplitude ratio obtained numerically by previously solving the motion of the needle at an interface of prescribed interfacial viscosity.

Consistency tests have been made by applying the aforementioned iterative scheme to numerically generated $[AR^*]^{pp}$ data for a $|\eta_s^*|$ in the range

$10^{-10} \leq |\eta_s^*| \leq 10^{-3}$ (Eq. (20)). The calculations have been made for the commercial needle described above in a cylindrical channel with $R = 10$ mm, at a frequency, $\omega = \pi$ rad/s.

Three cases are considered: purely viscous ($\eta_s^* = \eta_s' = \eta_s$), viscoelastic ($\eta_s^* = \eta_s' - \eta_s''i = \eta_s - \eta_s i$), and purely elastic interfaces ($\eta_s^* = -\eta_s''i = -\eta_s i$). The results are represented in Figure 5, where the left panels show the values of the real and imaginary parts of η_s^* obtained after convergence, namely $[\eta_s']_c$ (filled symbols) and $[\eta_s'']_c$ (open symbols), as a function of the prescribed value of η_s. The red line represents the perfect consistency line, $[\eta_s']_c = [\eta_s'']_c = |\eta_s|$. The top, middle, and bottom panels correspond, respectively, to the cases of purely viscous, viscoelastic, and purely elastic interfaces. The right panels in Figure 5 indicate, in each case, the number of iterations needed for convergence of the iterative process. The results are remarkably good in all cases except for in a small range of η_s values in the case of the purely elastic interfaces. Such an artifact has already been described for the case of the bicone bob rotational ISR [38, 39], probably due to a resonance phenomenon.

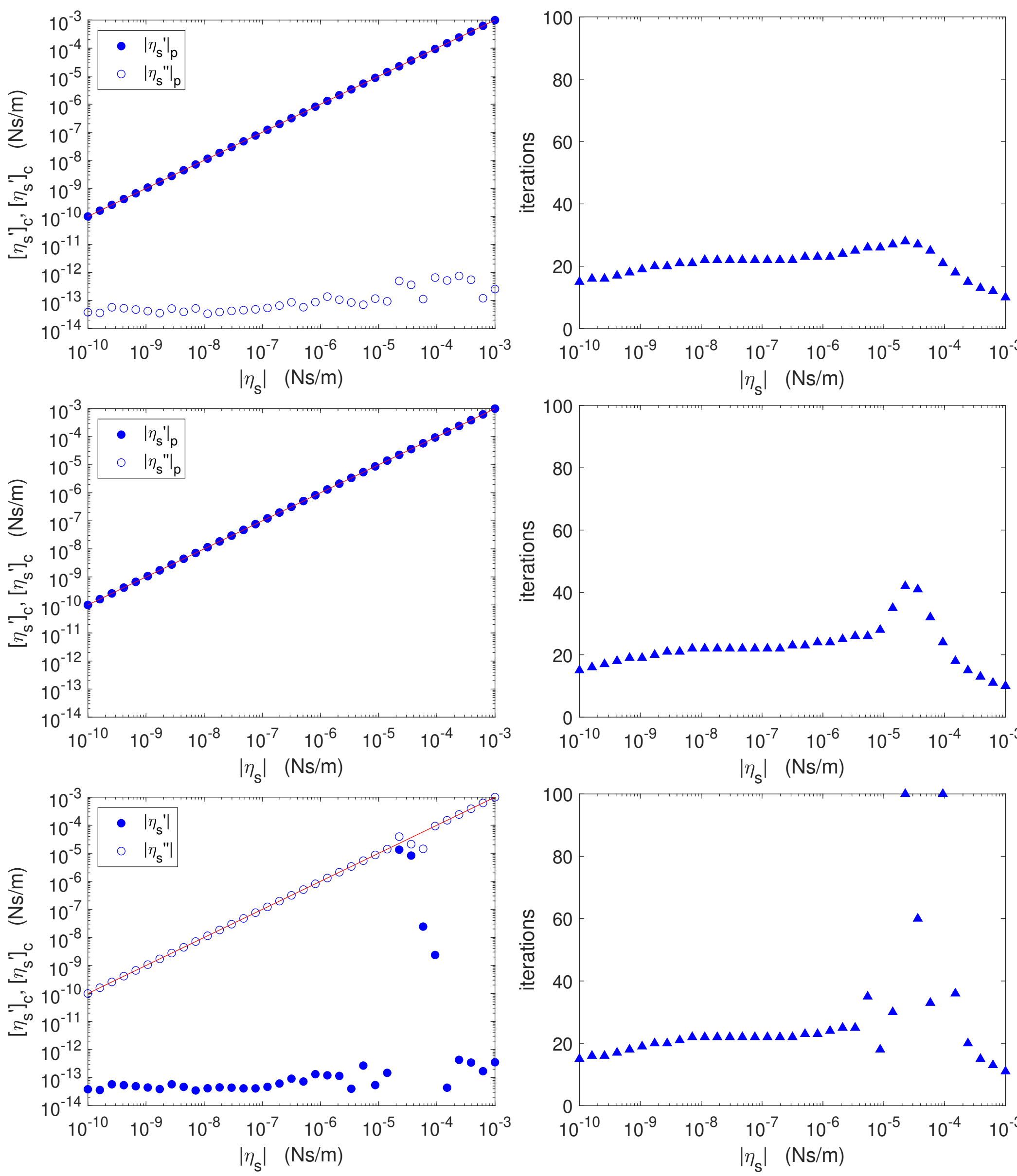

Figure 5: Results of the consistency test for the MTISR geometry (commercial needle at $\omega = \pi$ rad/s) for purely viscous (top row), viscoelastic (middle row), and purely elastic (bottom row) interfaces with real and imaginary parts of the complex interfacial viscosity in the range $10^{-10} < \eta_s < 10^{-3}$ Ns/m. Left panels: Comparison of the converged values $[\eta_s']_c$ (filled symbols), and $[\eta_s'']_c$ with the programmed value η_s (red line). Right panels: Number of iterations needed for convergence of the results in the corresponding left panel.

4. The Double wall-ring interfacial rheometer

The DWR geometry, shown in Figure 1c, was proposed by Vandebril et al. [22]. It takes advantage of the excellent control and measurement capabilities of modern digital rotational rheometers regarding torque and angular displacement. In such a design, the authors were able to put together many advantages from other geometries, such as: i) the small contact perimeter to area ratio (similar to the case of the MNISR or knife-edge geometries), and ii) the sharp edges that pin the interface, mantaining it in a horizontal plane (similar to the case of the bicone bob rotational rheometer). Moreover, rotational systems with circular symmetry do not suffer from end effects, an advantage regarding the MNISR which has a necessarily limited linear displacement range, and consequently allow to make not only oscillatory measurements but also continuous rotation measurements, such as viscometry or creep/recovery modes. Finally, the DWR geometry usually presents a smaller moment of inertia compared to the bicone bob probes, which is an advantage when working at high frequencies or short times. Interestingly, in the case of the DWR ISR, the corresponding flow field-based data analysis scheme was proposed simultaneously to the instrument design [22]. In the following we will mainly focus on the case of oscillatory excitation because, usually, it allows for a better separation of the viscous and elastic components of the sample's response.

4.1. The flow field-based data analysis scheme for the DWR

The physical model [22] assumed a horizontal and flat interface between two Newtonian fluids, pinned at the sharp edges at the channel and the ring. The flow velocity, both at the bulk phases and the interface, is supposed to have just one non null azimuthal component and to be purely axisymmetric. Under such assumptions, the Navier-Stokes equations for the azimuthal component of the velocity, in a cylindrical coordinate system with the origin at the center of the bottom surface of the channel, can be written as

$$\eta_j \left[\frac{\partial}{\partial r} \left(\frac{1}{r} \frac{\partial}{\partial r} (r v_j) \right) + \frac{\partial^2 v_j}{\partial z^2} \right] = \rho_j \frac{\partial v_j}{\partial t}, \tag{25}$$

where the subindex j refers to either of the bulk phases. Consequently, η_j and ρ_j represent, respectively, the dynamic viscosity and the density of the bulk phase j. Correspondingly, the boundary conditions are no-slip at the channel walls and floor, and free surface at the air/upper bulk phase interface

$$v_1(R_1, z) = v_2(R_2, z) = v_1(R_3, z) = v_2(R_4, z) = v_1(r, 0) = 0 \tag{26}$$

$$\left(\frac{\partial v_2(r, z)}{\partial z}\right)_{z=H_1+H_2} = 0, \tag{27}$$

and

$$v_j(R_5) = R_5\Omega, \tag{28}$$

$$v_j(R_6) = R_6\Omega, \tag{29}$$

at the ring surface, where Ω is the instantaneous angular velocity of the ring. Notice that it can represent either a rotational motion, if Ω is constant, or oscillatory motion, if $\Omega = i\theta_0\omega e^{i\omega t}$, where i is the imaginary unit, and θ_0 and ω the angular amplitude and frequency, respectively, of an oscillatory motion, $\theta(t) = \theta_0 e^{i\omega t}$.

In the case of the DWR configuration with two fluid phases, contributions from both bulk phases appear in the Boussinesq-Scriven boundary condition, that reads,

$$\eta_1 \frac{\partial v_1}{\partial z} - \eta_2 \frac{\partial v_2}{\partial z} = \pm \eta_s^* \frac{\partial}{\partial r}\left(\frac{1}{r}\frac{\partial}{\partial r}(r v_s)\right), \quad \text{at } z = H_1, \tag{30}$$

where the subscript s indicates physical quantities corresponding to the interface, and the $\pm$ signs correspond to the cases of the inner and outer parts of the interface, respectively. In the case of constant angular velocity and Newtonian interfaces the interfacial viscosity is a real parameter.

Next, the velocity field is assumed to be separable into a time dependent part, that follows the probe angular velocity Ω, and a spatially varying function, $a_j(r, z)$ that carries the spatial dependence of the velocity field at the interface and both bulk phases, namely,

$$v_j = a_j(r, z)\Omega. \tag{31}$$

The mathematical problem defined by the Navier-Stokes equations (25), the no-slip boundary conditions (27) and (29), the Boussinesq-Scriven condition at the interface (30), and the velocity field ansatz (31), can be discretized and solved numerically. The numerical solution for the velocity field can be used later on to calculate the total drag torque, M_c, comprising the interface and bulk phases contributions, from the following expression:

$$\begin{aligned} M_C = 2\pi\eta_s^* &\left[R_5^3 \frac{\partial}{\partial r}\left(\frac{v_s}{r}\right)\Big|_{r=R_5} - R_6^3 \frac{\partial}{\partial r}\left(\frac{v_s}{r}\right)\Big|_{r=R_6} \right] \\ &- 2\pi\eta_1 \left[\int_{R_5}^{R_r} \frac{\partial v_1}{\partial p_1} r^2 dr + \int_{R_r}^{R_6} \frac{\partial v_1}{\partial p_2} r^2 dr \right] \\ &- 2\pi\eta_2 \left[\int_{R_5}^{R_r} \frac{\partial v_2}{\partial p_3} r^2 dr + \int_{R_r}^{R_6} \frac{\partial v_2}{\partial p_4} r^2 dr \right], \end{aligned} \tag{32}$$

where R_r is the radial coordinate of the upper and lower vertexes of the ring, coordinates p_i are normal to the ring facets, and the contributions of the interface and both bulk phases are easily recognized. A complete description of the flow field configurations obtained with such a scheme and the overall instrument performance can be found in reference [22].

The calculated total drag torque, M_C, can be compared with the inertia corrected torque data given by most commercial rotational rheometers and, hence, it can be used to devise an iterative scheme to obtain the value of the complex interfacial viscosity. For instance, Vandebril et al. [22] proposed to use the simple scheme

$$[\eta_s^*]_{k+1} = [\eta_s^*]_k \frac{M_{exp}}{M_C^k}, \tag{33}$$

where M_{exp} is the inertia corrected torque yielded by the rotational rheometer. The MATLAB® implementation of this scheme has been made freely available by its authors at `https://softmat.mat.ethz.ch/opensource.html`

Such a scheme has been successfully exploited in experimental studies of interfacial systems such as polymer blends [57], particle laden interfaces [58, 59, 60], microgels [61], asphaltene films [62], tiled graphene oxide nanoflakes [63], protein films [64, 65, 66], protein-surfactant mixtures [67], CO_2 in water foams [68], amyloid biofilms [69], DPPC monolayers [52], cereal dough liquor [70, 71], and thermo-responsive polymers [72].

However, expression (33) is an ad-hoc choice that has no physical basis. This might bring problems because M_C^k is a nonlinear function of $[\eta_s^*]_k$ and, hence, there is no guarantee that the fixed points of the iterative map (33) are a proper solution for the problem. Opting for iterative schemes based on physical grounds should be advantageous. The equation of motion of the probe has been shown [38, 39] to be of great help for this purpose in the case of the bicone bob ISR. In the following subsection we show how to use the equation of motion of the probe to set up a physically founded iterative scheme for the DWR.

4.2. An alternative scheme for the DWR derived from the probe dynamics.

Let us, first, particularize the mathematical problem for the most usual case of oscillatory forcing, by making physical quantities non-dimensional, using R_6 and $1/\omega$ as characteristic length and time scales, and slightly modifying expression (31) so that now the ansatz for the velocity field is

$$v_j = g_j^*(r, z)\Omega R_6. \tag{34}$$

Notice that now the velocity amplitude function is non-dimensional. The choice of R_6 as the characteristic length scale is immaterial because any other length related to the ring would be equally adequate. Nevertheless, the choice of R_6 as the characteristic length scale is very convenient because it is the position at which the flow speed will take its highest value and, consequently, the value of the non-dimensional velocity amplitude function at the external rim of the ring will be $g^*(\bar{R}_6) = 1$. After the non-dimensionalization process and using expression (34), the Navier-Stokes equations for both bulk phases are (the overbars indicate non-dimensional quantities)

$$iRe_j g_j^*(\bar{r}, \bar{z}) = \frac{\partial}{\partial \bar{r}} \left(\frac{1}{\bar{r}} \frac{\partial}{\partial \bar{r}} \left(\bar{r} g_j^* \right) \right) + \frac{\partial^2 g_j^*}{\partial \bar{z}^2}, \tag{35}$$

where the Reynolds numbers for the bulk phases are $Re_j = \rho_j \omega R_6^2/\eta_j$. The boundary conditions are again no-slip at the channel walls and floor, and free surface at the air/upper bulk phase interface.

$$g_1^*(\bar{R}_1,\bar{z}) = g_2^*(\bar{R}_2,\bar{z}) = g_1^*(\bar{R}_3,\bar{z}) = g_2^*(\bar{R}_4,\bar{z}) = g_1^*(\bar{r},0) = 0, \tag{36}$$

$$\left(\frac{\partial g_2^*(\bar{r},\bar{z})}{\partial \bar{z}}\right)_{\bar{z}=\bar{H}_1+\bar{H}_2} = 0 \tag{37}$$

There must be no-slip boundary conditions at the ring contact lines, too

$$g_j^*(\bar{R}_5) = \bar{R}_5, \tag{38}$$

$$g_j^*(\bar{R}_6) = 1, \tag{39}$$

while the Boussinesq-Scriven boundary condition is written as

$$\frac{\partial g_1^*}{\partial \bar{z}} - \frac{1}{Y}\frac{\partial g_2^*}{\partial \bar{z}} = \pm N^* \frac{\partial}{\partial \bar{r}}\left(\frac{1}{\bar{r}}\frac{\partial}{\partial \bar{r}}(\bar{r} g_s^*)\right), \quad \text{at } \bar{z} = \bar{H}_1, \tag{40}$$

being $Y = \frac{\eta_1}{\eta_2}$ and $N^* = \frac{\eta_s^*}{\eta_1 R_6}$, as is done in reference [73]. Following [74], we define the complex Boussinesq number as: $Bo^* = \frac{\eta_s^*}{(\eta_1+\eta_2)R_6}$ so that the drag torque can be written in the following way

$$\begin{aligned}
M_C^* &= 2\pi i\omega\theta_0 e^{i\omega t} Bo^*(\eta_1+\eta_2)R_6^3 \left[\bar{R}_5^3 \frac{\partial}{\partial \bar{r}}\left(\frac{g_s^*}{\bar{r}}\right)\bigg|_{\bar{r}=\bar{R}_5} - \frac{\partial}{\partial \bar{r}}\left(\frac{g_s^*}{\bar{r}}\right)\bigg|_{\bar{r}=\bar{R}_6}\right] \\
&- 2\pi i\omega\theta_0 e^{i\omega t}\eta_1 R_6^3 \left[\int_{\bar{R}_5}^{\bar{R}_r} \frac{\partial g_1^*}{\partial \bar{p}_1}\bar{r}^2 d\bar{r} + \int_{\bar{R}_r}^{\bar{R}_6} \frac{\partial g_1^*}{\partial \bar{p}_2}\bar{r}^2 d\bar{r}\right] \\
&- 2\pi i\omega\theta_0 e^{i\omega t}\eta_2 R_6^3 \left[\int_{\bar{R}_5}^{\bar{R}_r} \frac{\partial g_2^*}{\partial \bar{p}_3}\bar{r}^2 d\bar{r} + \int_{\bar{R}_r}^{\bar{R}_6} \frac{\partial g_2^*}{\partial \bar{p}_4}\bar{r}^2 d\bar{r}\right] \\
&= M_s^* + M_1^* + M_2^*,
\end{aligned} \tag{41}$$

where coordinates p_i are normal to the ring facets, and, again, the contributions due to the interface, M_s^*, and both bulk phases, M_1^* and M_2^*, are easily identified. In this scheme, the above equations must be completed with the probe (rotor plus ring fixture ensemble) equation of motion. Since $\theta(t) = \theta_0 e^{i\omega t}$ and the total applied torque, without inertia correction, is supposed to be $M^*(t) = M_0 e^{i(\omega t-\delta)}$, the equation of motion for the probe is

$$I\ddot{\theta} + M_C^* = M_0 e^{i(\omega t-\delta)}. \tag{42}$$

Furthermore, the complex amplitude ratio between the (measurable) total applied torque and the angular position can be written as:

$$\begin{aligned}
AR^* &= \frac{M_0 e^{i(\omega t-\delta)}}{\theta_0 e^{i\omega t}} = \frac{M_0}{\theta_0} e^{-i\delta} = \frac{M_s^* + M_1^* + M_2^* - I\omega^2 \theta_0 e^{i\omega t}}{\theta_0 e^{i\omega t}} = \\
& i\omega 2\pi Bo^* (\eta_1 + \eta_2) R_6^3 \left[\bar{R}_5^3 \frac{\partial}{\partial \bar{r}} \left(\frac{g_s^*}{\bar{r}} \right) \Big|_{\bar{r}=\bar{R}_5} - \frac{\partial}{\partial \bar{r}} \left(\frac{g_s^*}{\bar{r}} \right) \Big|_{\bar{r}=\bar{R}_6} \right] \\
& + i\omega 2\pi R_6^3 \left(\eta_1 \bar{M}_1^* + \eta_2 \bar{M}_2^* \right) - I\omega^2,
\end{aligned} \tag{43}$$

which, upon solving for the complex Boussinesq number, Bo^*, can be used to set up the following iterative scheme:

$$[Bo^*]_{k+1} = \frac{AR_{exp}^* - i\omega 2\pi R_6^3 \left(\eta_1 \left[\bar{M}_1^* \right]_k + \eta_2 \left[\bar{M}_2^* \right]_k \right) + I\omega^2}{i\omega 2\pi (\eta_1 + \eta_2) R_6^3 \left[\bar{M}_s^* \right]_k}, \tag{44}$$

where the non-dimensional drag torques are:

$$\begin{aligned}
\left[\bar{M}_s^* \right]_k &= \bar{R}_5^3 \frac{\partial}{\partial \bar{r}} \left(\frac{[g_s^*]_k}{\bar{r}} \right) \Big|_{\bar{r}=\bar{R}_5} - \frac{\partial}{\partial \bar{r}} \left(\frac{[g_s^*]_k}{\bar{r}} \right) \Big|_{\bar{r}=\bar{R}_6}, \\
\left[\bar{M}_1^* \right]_k &= \int_{\bar{R}_5}^{\bar{R}_r} \frac{\partial [g_1^*]_k}{\partial \bar{p}_1} \bar{r}^2 d\bar{r} + \int_{\bar{R}_r}^{\bar{R}_6} \frac{\partial [g_1^*]_k}{\partial \bar{p}_2} \bar{r}^2 d\bar{r}, \\
\left[\bar{M}_2^* \right]_k &= \int_{\bar{R}_5}^{\bar{R}_r} \frac{\partial [g_2^*]_k}{\partial \bar{p}_3} \bar{r}^2 d\bar{r} + \int_{\bar{R}_r}^{\bar{R}_6} \frac{\partial [g_2^*]_k}{\partial \bar{p}_4} \bar{r}^2 d\bar{r}.
\end{aligned} \tag{45}$$

Such a scheme does not rely on the rheometer's automatic inertia correction. A comparative study, in terms of the number of iterations needed for convergence, the total processing time, and the numerical consistency between both formulations of the iterative process, would be of significant practical interest.

To conclude this section we would like to mention briefly that Lopez and Hirsa [75] proposed an elegant approach to the hydrodynamic problem, based on a stream function and vorticity formulation. Such an approach allows one to find the full three dimensional configuration of the velocity field for the knife-edge ISR and the DWR ISR. It is appealing to apply such a formulation to build a flow field-based data analysis scheme for both types of ISR by finding the solution of the full 3D velocity field, supplementing it with the calculation of the interfacial and subphase drag torques, and setting up an iterative scheme that might have a higher accuracy than the simple single velocity component schemes here mentioned. Such an scheme will have the obvious drawback of demanding larger computational times.

5. The oscillating conical bob

The bicone bob is one of the oldest geometries still in use in the implementation of interfacial shear rheometers based on stress controlled rotational bulk rheometers (see, for instance, [16, 21] and references therein). Among the interfacial shear rheometers built on rotational bulk rheometers the DWR [36] typically offers higher values of Bo^* and better resolution than the bicone ones, due to its smaller area of contact with the subphase. However, the bicone bob geometry is a convenient and popular entry point into interfacial shear rheology for many experimental groups having a stress controlled rheometer because of the simplicity of the elements needed to set it up [37]. Not surprisingly, the bicone geometry is still widely used, e.g, in the study of biofilms [76, 77, 78], PMMA and colloidal polystyrene latex quasi-monolayers [79], differences between proteins and surfactants [80], interfacial layers of cellulose nanocrystals [81], emulsifiers (e.g., chitosan) [82], polyhydroxyalkanoate degradation at interfaces [83], or interfacial network formation induced by crystalization [84].

Common to all interfacial rheometers is the challenge of extracting accurate values for the rheological parameters out of the experimental data, mainly due to the strong coupling between the interfacial and bulk flow. In the case of the bicone geometry there is an extreme need to separate the interfacial and subphase contributions of the system response because of the large contact area of the probe with the subphase. Consequently, considerable effort has been made in the past to obtain analytical models that might be useful to unravel the rheological information contained in the experimental data for different geometrical and dynamical configurations.

Soo-Gun and Slattery [73] provided an exact solution for the case of a zero-thickness disk pending from a torsion wire, with the fluid-containing cup rotating at a constant angular velocity. Later on, the work of Soo-Gun and Slattery [73] was adapted to the case where the cup performs angular oscillations at a given frequency by Ray et al. [85] and Nagarajan et al. [86]. However, nowadays, the most used configuration consists on the conical bob being fixed to the moving rotor of a stress controlled rotational rheometer. During dynamical measurements in this configuration, an oscillating torque is applied to the rotor plus probe assembly, and its angular displacement is measured. Erni et al. [74] adapted the exact solution in [73] to the stress controlled oscillating bob system by imposing appropriate boundary conditions and recasting the constant angular velocity into an oscillatory angular velocity. However, the validity of such an approach is limited to situations in which the vertical velocity profile in the subphase is linear, which demands small subphase depths, low frequencies, and/or moderate viscosity subphase fluids. A detailed analysis of the flow field configurations in the oscillating cup and oscillating bob configurations can be found in [37].

Tajuelo et al. [37] transposed the ideas from Reynaert et al. [35] and Verwijlen et al. [36] to the case of the oscillating bob in the stress controlled mode. In this configuration, the experimental data usually consists on the complex amplitude ratio, AR^*, between the total imposed torque and the angular displacement of the rotor+bicone assembly. The experimental disposition of the interfacial oscillating bob is depicted in Figure 1c.

The rheometer consists of a conical bob, connected to the rheometer rotor, that is level with the air/water interface. The bulk fluid subphase is contained in a cylindrical cup having its axis aligned with the cylindrical symmetry axis of the bob (see Fig.1c). The surface is considered horizontal and having null-thickness, and the flow field is assumed to have only one non null velocity component in the azimuthal direction, v_θ. For such a configuraton, the Navier-Stokes equations in cylindrical coordinates read:

$$\frac{\partial v_\theta}{\partial t} = \frac{\eta}{\rho}\left(\frac{\partial^2 v_\theta}{\partial r^2} + \frac{\partial^2 v_\theta}{\partial z^2} + \frac{1}{r}\frac{\partial v_\theta}{\partial r} - \frac{v_\theta}{r^2}\right), \tag{46}$$

where ρ and η are the density and the viscosity of the bulk fluid subphase, respectively, and r and z the radial and vertical direction coordinates, respectively. The rotor is supposed to oscillate at a constant frequency, ω, with an angular amplitude, θ_0, so that $\theta(t) = \theta_0 e^{i\omega t}$. It is further assumed that the fluid velocity at any point will be proportional to the velocity of the points at the bicone rim, so that the temporal and spatial dependencies of the velocity field can be separated as

$$v_\theta(r,z,t))\theta(t) = v_{\theta,b}(t) g^*(r,z), \tag{47}$$

where $v_{\theta,b}(t)$ is the velocity of the points at the bicone rim,

$$v_{\theta,b}(t) = i\omega R_b \theta_0 e^{i\omega t}, \tag{48}$$

and $g^*(r,z)$ is a nondimensional amplitude of the velocity field, which is a complex function whose real and imaginary parts are in phase and out of phase with the bicone velocity. Making spatial coordinates nondimensional, by using the cup radius as the characteristic length scale, the Navier-Stokes equation for this problem (46) can be written as follows:

$$i\,Re\,g^*(\bar{r},\bar{z}) = \frac{\partial^2 g^*(\bar{r},\bar{z})}{\partial \bar{r}^2} + \frac{\partial^2 g^*(\bar{r},\bar{z})}{\partial \bar{z}^2} + \frac{1}{\bar{r}}\frac{\partial g^*(\bar{r},\bar{z})}{\partial \bar{r}} - \frac{g^*(\bar{r},\bar{z})}{\bar{r}^2}. \tag{49}$$

Here the Reynolds number is defined as $Re = \rho\omega R_c^2/\eta$, where ρ and η are the bulk density and viscosity, respectively, ω is the oscillating frequency, and R_c is the cup radius.

Boundary conditions are no-slip at the cup floor and lateral walls, and at the bicone-subphase contact area. Moreover, null fluid velocity is assumed a at points located along the vertical symmetry axis, i.e.,

$$\begin{aligned}
&g^*(\bar{r},0) = g^*(1,\bar{z}) = 0,\\
&g^*(0,\bar{z}) = 0,\\
&g^*(\bar{r} \le \bar{R}_b, \bar{h}) = \frac{\bar{r}}{\bar{R}_b}.
\end{aligned} \tag{50}$$

Moreover, the Boussinesq-Scriven boundary condition applies at the interface and, in cylindrical coordinates and in non-dimensional form, reads:

$$\frac{\partial g^*}{\partial \bar{z}} = Bo^* \frac{\partial}{\partial \bar{r}}\left(\frac{1}{\bar{r}}\frac{\partial}{\partial \bar{r}}\left(\bar{r}\,g^*\right)\right)\text{, at } \bar{R}_b < \bar{r} < 1,\ \bar{z} = \bar{h}, \tag{51}$$

where the complex Boussinesq number is defined as

$$Bo^* = \frac{\eta_s^*}{R_c \eta}. \tag{52}$$

Next, the angular displacement and the torque exerted by the instrument are related through the equation of motion of the rotor+bicone assembly which reads

$$M^*(t) + M^*_{sub}(t) + M^*_{surf}(t) = I\frac{\partial^2\theta(t)}{\partial t^2}, \tag{53}$$

where $M^*(t)$ is the torque applied by the instrument, $M^*_{sub}(t)$ and $M^*_{surf}(t)$ are the drag torques imposed by the subphase and interface, respectively, and I is the moment of inertia of the rotor+bicone assembly. Incidentally, many commercial rotational rheometers perform an inertia correction over experimental data. When working with the full equation of motion (53), non inertia corrected (raw) data must be used. Conversely, the inertia term in equation (53) may be dropped when working with inertia-corrected torque data, hence, applying just a torque balance condition.

The interfacial and bulk subphase drag torques can be calculated from the horizontal and vertical velocity gradients of the velocity field. Written in terms of g^*, the corresponding expressions are:

$$\begin{aligned} M^*_{sub} &= -i\omega 2\pi R_b \eta\theta_0 e^{i\omega t}\int_0^{R_b} r^2 \left(\frac{\partial g^*}{\partial z}\right)\bigg|_{z=h} dr, \\ M^*_{surf} &= i\omega 2\pi R_b^2 R_c\, Bo^* \eta\theta_0 e^{i\omega t}\left(R_b\left(\frac{\partial g^*}{\partial r}\right)\bigg|_{r=R_b,\, z=h} - 1\right). \end{aligned} \tag{54}$$

In this scheme the next step consists in assuming that the torque exerted by the instrument is an oscillation with frequency ω with a certain phase lag with respect to the angular displacement, i.e.,

$$M^*(t) = M_0 e^{i(\omega t-\delta)} = M_0^* e^{i\omega t} \tag{55}$$

The main output data of modern rotational rheometers is just the time series corresponding to the time evolution of the applied torque and the angular displacement. Then, a complex amplitude ratio,

$$AR^*_{exp} = \frac{M^*_{exp}(t)}{\theta_{exp}(t)} = \frac{M_0}{\theta_0}e^{-i\delta}, \tag{56}$$

can be easily constructed. An equivalent definition of a theoretical amplitude ratio, using the applied torque and the angular displacement, followed by the substitution of expressions (54) into Eq.(53) leads to the following relation between AR^* and the spatial flow field configuration:

$$AR^* = i\omega 2\pi R_b \eta \left[\int_0^{R_b} r^2 \left(\frac{\partial g^*}{\partial z} \right) \bigg|_{z=h} dr \right.$$
$$\left. - R_b R_c \, Bo^* \left(R_b \left(\frac{\partial g^*}{\partial r} \right) \bigg|_{r=R_b,\, z=h} - 1 \right) \right] - I\omega^2. \tag{57}$$

Hence the question is: given an experimental value of AR^*, what is the value of the complex Boussinesq number, Bo^*, that solves the problem defined by Eqs. (49), (50), (51) coupled to (57)? Once that problem is solved, the complex interfacial viscosity can be found right away from (52), as $\eta_s^* = R_c \, \eta \, Bo^*$. However, the complex interfacial viscosity is also implicitly contained in the g^* calculation (Boussinesq-Scriven boundary condition, Eq. (51)). More precisely, equation (57) can be solved for Bo^* if one knows the gradients of the complex velocity amplitude function, but to find such gradients one needs to know the value of Bo^* in order to solve the hydrodynamic problem with the Boussinesq-Scriven boundary condition, equation (51).

Hence, it is necessary to resort to an iterative scheme. A first version of such an iterative scheme [37] was devised along the lines developpd in Reynaert et al. [35] and Verwijlen et al. [36], iterating over Bo^*, starting from a suitable value and using the experimental value of the amplitude ratio, AR^*_{exp}, as follows:

$$[Bo^*]_{k+1} = \frac{AR^*_{exp}}{AR^*_{calc}} [Bo^*]_k. \tag{58}$$

However, recently Sánchez-Puga et al. [39] proposed a different scheme, based on the same arguments here used is Subsection 4.2, that was based on solving equation (57) for Bo^*, so that

$$[Bo^*]_{k+1} = \frac{-AR^*_{exp} - I\omega^2 + i\omega 2\pi R_b \eta \int_0^{R_b} r^2 \left(\frac{\partial [g^*]_k}{\partial z} \right) \Big|_{z=h} dr}{R_b R_c \left(R_b \left(\frac{\partial [g^*]_k}{\partial r} \right) \Big|_{r=R_b,\, z=h} - 1 \right)}. \tag{59}$$

In this scheme, thoroughly described in Sánchez-Puga et al. [39], one starts from an appropriate seed, for instance, the Bo^* value corresponding to a linear interfacial velocity profile, or the solution of the hydrodynamic problem corresponding to a clean interface, $Bo^* = 0$. Then, the gradients of the complex velocity amplitude function are introduced in equation (59), and a new value of Bo^* is found. The scheme is iterated till convergence is achieved.

The condition for convergence might be defined on the successive values of Bo^*. However, since the experimental observable being the complex amplitude ratio, we have chosen to stipulate it on the successive values of AR^*, as follows

$$\left| \frac{[AR^*_{calc}]_k - AR^*_{exp}}{AR^*_{exp}} \right| \leq tolMin, \tag{60}$$

where $[AR^*_{calc}]_k$ is the numerically calculated value for AR^* in the k-th iteration, and $tolMin$ is the user-defined threshold tolerance. MATLAB® (or GNU Octave) and Python3® versions of the code to solve the full iterative scheme, including the hydrodynamic calculations, have been made publicly available by the authors at [39].

We will briefly illustrate the performance of this scheme by showing some results obtained for the case of a bicone with radius $R_b = 34$ mm, in a cup with radius $R_c = 40$ mm, with a water lower bulk phase with depth $H = 10$ mm, and a forcing frequency $\omega = \pi$ rad/s. Such values are typical of the experimental realizations [37]. Full details on the second order centered finite difference numerical scheme used to solve the hydrodynamic problem can be found in Sánchez-Puga et al. [39].

First we show the results of some convergence tests performed on the hydrodynamic computations by varying the spatial resolution (mesh spacing) for a clean air/water interface ($Bo^* = 0$). The results using different rectangular meshes with $N \times M$ nodes (with $N = 2M$) are shown in Figure 6. The values of N and M have been chosen so that a node falls exactly at the bicone rim. The left panel of Figure 6 illustrates the dependency of the values of the real (blue line and symbols) and imaginary (red line and symbols) parts of the total torque of hydrodynamic origin ($M^*_{tot} = M^*_{sub} + M^*_{surf}$) acting on the rotor+bicone assembly. Very good convergence is attained for $N \geq 2000$. The right panel of Figure 6 shows the time needed to obtain the flow field configuration for the clean air/water interface as a function of N, when computed in a desktop computer having a Pentium Core i5-4460 microprocessor and 16 Gb RAM, with the MATLAB® code using the sparse matrix routines. The computation time per flow field configuration grows as N^2 but remains quite manageable even for high resolutions meshes (for $N = 1000$, $t_s \sim 4$ s).

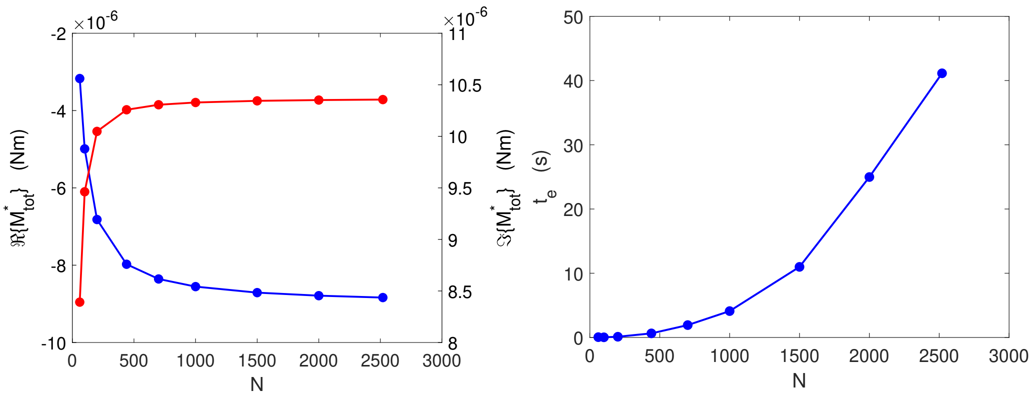

Figure 6: Left panel: Convergence of the real (blue trace) and imaginary (red trace) parts of the torque M^*_{tot} as a function of mesh size for a clean interface ($Bo^* = 0$). Right panel: time needed to solve the hydrodynamic problem to obtain the flow field configuration as a function of mesh size.

To illustrate how the mesh size affects the dynamical variables we have computed the relative differences in the real and imaginary parts of the total torque for the solutions obtained with three mesh sizes: 200×100, 440×220 and 1000×500 taking as a reference the solution for the 2520 × 1260 mesh size. More specifically, we have computed

$$[\Delta_r(\Re(M^*_{tot}))]_{N\times M} = \left| \frac{\Re((M^*_{tot})_{N\times M}) - \Re((M^*_{tot})_{2520\times 1260})}{\Re((M^*_{tot})_{2520\times 1260})} \right|, \qquad (61)$$

and

$$[\Delta_r(\Im(M^*_{tot}))]_{N\times M} = \left| \frac{\Im((M^*_{tot})_{N\times M}) - \Im((M^*_{tot})_{2520\times 1260})}{\Im((M^*_{tot})_{2520\times 1260})} \right|, \qquad (62)$$

for purely viscous interfaces with η_s in the range $10^{-6} \leq \eta_s \leq 1$ Ns/m, and at the same frequency, $\omega = \pi$ rad/s. The results are shown in Fig. 7.

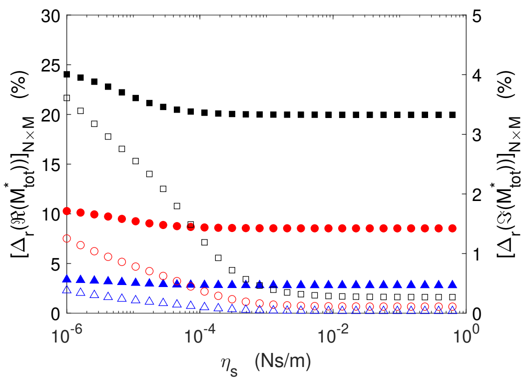

Figure 7: Relative differences in the real part, $\Delta_r(\Re(M^*_{tot}))$ (solid symbols), and imaginary part, $\Delta_r(\Im(M^*_{tot}))$ (open symbols), of the total torque between the solutions obtained with different mesh sizes taking as a reference the 2520×1260 mesh solution. Black symbols: 200×100 mesh. Red symbols: 440×220 mesh. Blue symbols: 1000×500.

For the case of the 1000×500 mesh (blue symbols), the relative difference with the finest mesh is always below 5% in the real part (solid symbols) and below 0.5% in the imaginary part (open symbols). The 1000×500 mesh represents, therefore, a good compromise between resolution and computational costs, comprising memory availability and computational time (approximately 5 s per flow field configuration solved for the 1000×500 nodes mesh against 55 s for the 2520×1260 nodes mesh).

In Figure 8 we show color coded plots of the real and imaginary parts of the velocity amplitude function, $\Re[g^*(r,z)]$ (left panel), and $\Im[g^*(r,z)]$ (right panel), respectively. The flow fields were calculated for $Bo^* = 0.1 - 0.1i$ with a 2520×1260 mesh. Strong velocity gradients can be appreciated in the subphase close to the bicone surface and at the interface. Notice that the values of $\Re[g^*(r,z)]$ are very small everywhere but in a very small neighborhood of the bicone surface, which is located at the top row of the images, spanning from $r = 0$ to $r = 34$ mm.

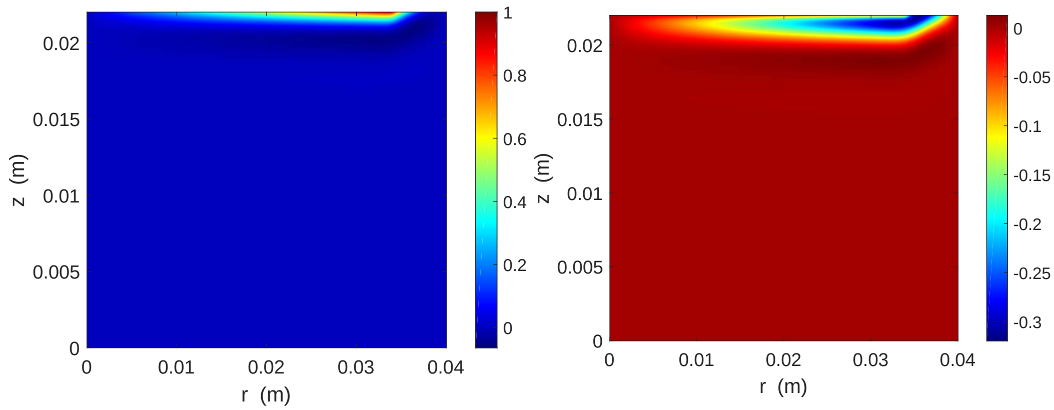

Figure 8: Color coded plots of (a) $\Re[g^*(r,z)]$, and (b) $\Im[g^*(r,z)]$ at $Bo^* = 0.1 - 0.1i$ and $\omega = \pi$ rad/s.

To illustrate the influence of the values of Bo^* and ω on the interfacial velocity profile, $g_s^*(r) = g^*(R_b < r < R_c, z = h)$, we show in Figure 9 some interfacial velocity profiles obtained in calculations performed with a mesh of 2520×1260 nodes, for three different conditions. Case A (black lines) stands for a viscoelastic interface with $\eta_s^* = (1-i) \times 10^{-3}$ Ns/m at moderately high frequency, $\omega = 10\pi$ rad/s. Case B (red lines) corresponds to a purely viscous interface, $\eta_s^* = 10^{-5}$ Ns/m, at an intermediate frequency, $\omega = \pi$ rad/s. Case C refers to a clean interface, $\eta_s^* = 0$ Ns/m, at low frequency, $\omega = \pi/10$ rad/s. Continuous lines correspond to the real part of the velocity amplitude function at the interface, $\Re[g_s^*(r)]$, and the dashed lines to the imaginary part of the same function, $\Im[g_s^*(r)]$. We also plot the analytical solution corresponding to $|Bo^*| \to \infty$, that has been obtained by considering an interface fully decoupled from the subphase, i.e., neglecting the bulk contribution to the interfacial shear stress balance (left hand side in expression (51)). In this configuration, the nondimensional analytical solution of equation (51) for $|Bo^*| \to \infty$ is [75]

$$g_s(\bar{r}) = \frac{\bar{R}_b\left(\bar{r}^2 - 1\right)}{\bar{r}\left(\bar{R}_b^2 - 1\right)} = \frac{\bar{R}_b}{\bar{R}_b^2 - 1}\left(\bar{r} - \frac{1}{\bar{r}}\right), \tag{63}$$

which in all configurations with small bicone rim-to-cup wall distance compared to the bicone radius (as is the case here: $R_c - R_b = 6$ mm, $R_c = 40$ mm; $\bar{R}_b = 0.85$) is quite close to a linear profile.

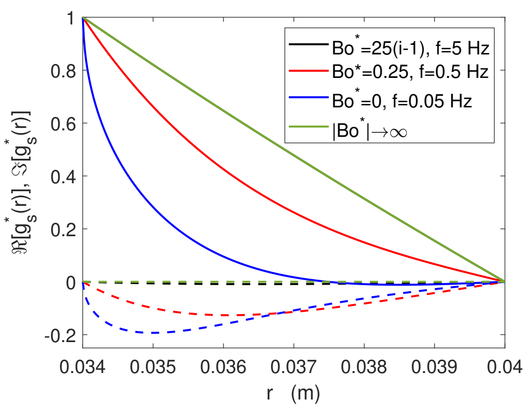

Figure 9: Real and imaginary parts of $g_s^*(r)$ at different ω and Bo^* values. Continuous and dashed lines represent the real and imaginary parts, respectively. Case A: High frequency with a viscoelastic interface (black); case B: Medium frequency with purely viscous interface (red); case C: Low frequency and clean air-water interface (blue). $|Bo^*| \to \infty$ analytical solution (green line). Continuous lines: $\Re[g_s^*(r)]$; dashed lines: $\Im[g_s^*(r)]$

Case A corresponds to a high $|Bo^*|$ situation and, consequently, the real part of the velocity amplitude function is close to the analytical solution given in equation (63), and the imaginary part is close to zero. As the value of $|Bo^*|$ decreases, strongly nonlinear radial gradients appear on g_s^* with non null imaginary parts, as is clearly illustrated by the graphs corresponding to cases B and C in Figure 9.

In order to study the consistency [38, 39] of the iterative scheme to obtain the converged value of the complex Boussinesq number and, consequently the value of η_s^*, we have performed a two step process: i) solving the fluid dynamical problem for different values of the complex interfacial viscosity and computing the corresponding amplitude ratio, AR^*, and ii) feeding the iterative process with the AR^* values found in order to obtain the converged value of the complex Boussinesq number and, consequently, the converged value of η_s^*. All computations have been made on the same system geometry considered up to here and at the same frequency.

We have applied such a procedure to interfaces that are purely viscous, with $\eta_s^* = \eta_s$, viscoelastic, with $\eta_s' = \eta_s'' = \eta_s$ (i.e., $\eta_s^* = (1-i)\eta_s$), and purely elastic, with $\eta_s^* = -i\eta_s$. The values of η_s have spanned the range $10^{-7} \leq \eta_s \leq 1$ Ns/m and we have recorded the corresponding number of iterations needed to achieve convergence. The results are represented in Figure 10, where the left panels show the values of the real and imaginary parts of η_s^* obtained after convergence, namely $[\eta_s']_c$ (filled symbols) and $[\eta_s'']_c$

(open symbols), as a function of the programmed value of η_s. The red line represents the perfect consistency line, $[\eta_s']_c = [\eta_s'']_c = |\eta_s|$. Top, middle, and bottom panels correspond, respectively, to the cases of purely viscous, viscoelastic, and purely elastic interfaces. The right panels in Figure 10 indicate, in each case, the number of iterations needed for convergence of the iterative process.

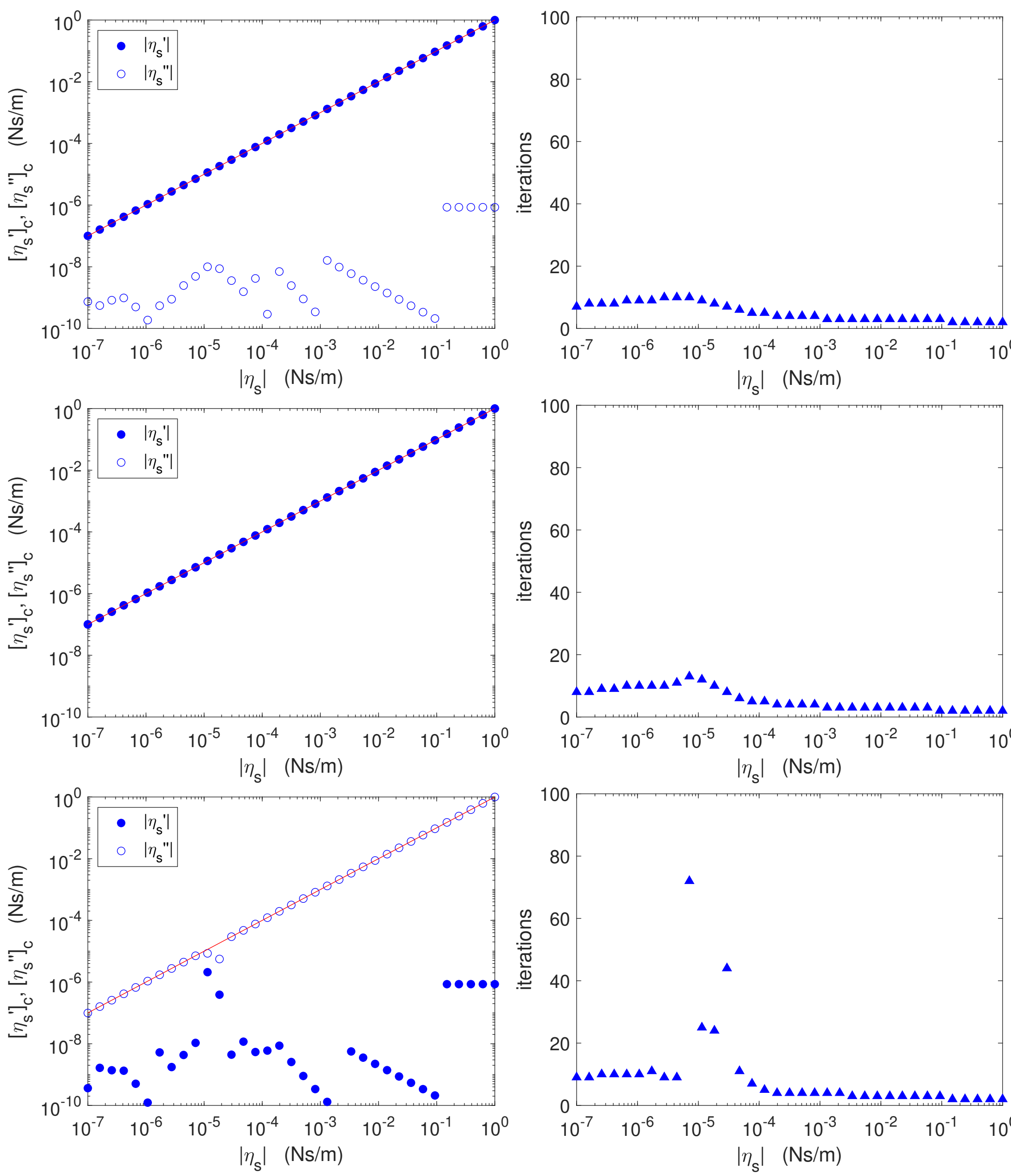

Figure 10: Results of the consistency test of the bicone geometry ($R_m = 10$ μm and $\omega = \pi$ rad/s) for purely viscous (top row), viscoelastic (middle row), and purely elastic (bottom row) interfaces with real and imaginary parts of the complex interfacial viscosity in the range $10^{-7} < \eta_s < 1$ Ns/m. Left panels: Comparison of the converged values $[\eta_s']_c$ (filled symbols), and $[\eta_s'']_c$ with the programmed value η_s (red line). Right panels: Number of iterations needed for convergence for the results in the corresponding left panel.

For the purely viscous interfaces (top row), the value of η_s' is nicely recovered, while numerical errors yield a value of η_s'' that is always at least two orders of magnitude smaller than the value of η_s'. For the viscoelastic interfaces (middle row), both the real and imaginary parts of the complex interfacial viscosity are recovered by the iterative process with high precision. For the purely elastic interfaces (bottom row), the value of η_s'' is nicely recovered, while numerical errors yield a value of η_s' that is always at least two orders of magnitude smaller than the value of η_s'. The only exception is a small region at approximately $\eta_s = 10^{-5}$ Ns/m, where a resonance effect disturbs the data analysis procedure [38, 39]. The plots of the number of iterations needed for convergence are very similar to each other in the three cases considered, varying between 2 and 100 iterations in the full complex viscosity range here studied.

To estimate the resolution of a particular instrument, a specific study of the impact of the measurement uncertainties (in the torque and the angular displacement) of the instrument on the output η_s^* values should be carried out. Different aspects of such a study, for the case of the Bohlin C-VOR instrument with purposely built conical bob and cup, may be found in [37, 38, 39].

Although we will not make a detailed discussion of the case of rotational rheometers working in controlled strain mode, some comments can be anticipated. The analysis of experimental results on very soft samples obtained in rheometers working in controlled strain mode (systems with separate motor transducer, in the terminology of reference [11]) must be made with care, particularly in the case of low viscosity subphases (such as water). In such systems, a motor drives one part of the geometry (typically the external cup, which includes the bottom plate) while the hydrodynamic torque is measured at the other part (for instance, the upper rotor plus bicone/ring assembly). In such a case, the viscous length scale, ℓ_ω, at the subphase rules the transfer of momentum from the oscillating cup towards the probe, while the interfacial viscous length scale, ℓ_ω^s, rules the transfer of momentum from the lateral wall of the cup towards the probe rim through the interface. In other words, in an upwards frequency sweep one might go from a linear vertical velocity profile situation ($\ell_\omega > H_1$) to a nonlinear vertical velocity profile one ($\ell_\omega < H_1$).

This happens, for instance, for a water subphase with a depth typically used in the bicone or DWR ISRs ($H_1 \sim 1$ cm). Consequently, the condition for having a linear vertical velocity profile is fulfilled only if $\omega \leq 10{-}2$ rad/s. Hence, in most practical situations such condition is not fulfilled, the vertical velocity profile in the subphase is not linear, and only an adequate flow field-based data analysis can properly obtain the interfacial rheological parameters out of the experimental data in such a situation. Decreasing the gap might bring back the system to a linear vertical velocity profile condition but at the expense of increasing the subphase drag torque while keeping the interfacial drag torque unchanged and, consequently, loosing instrument's sensitivity. Anyway, modifying the flow field-based scheme here sketched for the bicone case (Section 5) to fit the separate motor transducer configuration merely amounts to a change in the boundary conditions at the probe surface (at rest) and at the cup's floor and lateral walls (oscillating). This should be a rather straightforward modification of the code and should deal smoothly with the eventually nonlinear interfacial and subphase flow configurations.

6. Extensions of the techniques

In this section we will briefly outline some extensions of the above discussed techniques to different open problems.

6.1. Flow field-based data analysis for the microbutton ISR

A very elegant and highly sensitive interfacial rheometer based on rotating microfabricated probes (microbuttons) was proposed and developed by the Santa Barbara group [23, 24, 25, 26]. The probes are ferromagnetic, they are subject to a magnetic torque generated by externally controlled electromagnets, and their position and orientation is measured by an image tracking system in real time. The data analysis is carried out by using the expressions obtained by Hughes et al. [41], in their analysis of the rotational drag on a cylinder moving in a membrane, which implicitly means that the interface and subphase motions are assumed to be decoupled from each other, i.e., such approximation is strictly valid only for $Bo >> 1$.

Interestingly, the fluid mechanical problem for the microbutton is very similar to the bicone one [37, 39], and the scheme mentioned in the previous section for the bicone could conceivably be applied to the microbutton system [26] right away. However, a careful consideration of the probe and cup sizes, and the interfacial and bulk viscous length scales [46] shows that a rectangular mesh should be excedingly fine in order to adequately resolve the flow structure close to the microbutton rim, at the interface, and under the microbutton, at the bulk subphase. Hence, it is convenient to use logarithmic variables in the radial and vertical directions in order to achieve better resolution close the microbutton with manageable mesh sizes and computation times.

For the sake of completeness we will directly present the formulation of the problem corresponding to a geometry including two bulk phases under oscillatory forcing. Using logarithmic variables in such a configuration makes it necessary to place the vertical coordinate origin in the plane were the microbutton is located, and making the vertical coordinate to be positive downwards in the lower bulk phase (1), and positive upwards in the upper bulk phase (2). With this choice, the signs of the derivatives in the equations for the lower bulk phase and in the boundary condition at the interface must be properly taken care of.

We start the formulation of the mathematical problem by using the button rim velocity in the velocity ansatz for this problem. We assume that the microbutton, with radius R_m, performs an oscillatory motion with angular displacement amplitude, Ω, and frequency, ω, so that $\Omega(t) = i\omega\theta_0 e^{i\omega t}$. Then, the velocity field at the bulk phase j is assumed to be separable in spatial and temporal components as follows

$$v_j = g_j^*(\bar{r}, \bar{z})\Omega R_m. \tag{64}$$

The non-dimensional Navier-Stokes equations in regular cylindrical coordinates for such a motion are

$$iRe_1 g_1^* = \frac{\partial^2 g_1^*}{\partial \bar{r}^2} + \frac{1}{\bar{r}}\frac{\partial g_1^*}{\partial \bar{r}} - \frac{g_1^*}{\bar{r}^2} + \frac{\partial^2 g_1^*}{\partial \bar{z}^2}, \tag{65}$$

$$iRe_2 g_2^* = \frac{\partial^2 g_2^*}{\partial \bar{r}^2} + \frac{1}{\bar{r}}\frac{\partial g_2^*}{\partial \bar{r}} - \frac{g_2^*}{\bar{r}^2} + \frac{\partial^2 g_2^*}{\partial \bar{z}^2}, \tag{66}$$

where the Reynolds number at each bulk phase is $Re_j = \rho_j \omega_j R_m^2/\eta_j$, and the spatial variables have been made non-dimensional by using the following transformations

$$\begin{aligned} \bar{r} &= \frac{r}{R_m}, & 0 \le \bar{r} \le \frac{R}{R_m} = \bar{R} \\ \bar{z} &= \frac{z}{R_m}, & -\frac{h}{R_m} \le \bar{z} \le \frac{h}{R_m} = \bar{h} \end{aligned}$$

Notice that for the microbutton probe Re_j will be very small, even in the case of low viscosity fluid phases, so that, for many practical purposes, the left hand side of equations (65) and (66) might be discarded. At the interface, the boundary condition is the usual Boussinesq-Scriven condition that now reads

$$N^* \frac{\partial}{\partial \bar{r}} \left(\frac{1}{\bar{r}} \frac{\partial}{\partial \bar{r}} \left(\bar{r} g_s^* \right) \right) = \frac{1}{Y} \frac{\partial g_2^*}{\partial \bar{z}} - \frac{\partial g_1^*}{\partial \bar{z}} \tag{67}$$

where we have defined parameters N^* and Y as in reference [73].

$$\begin{aligned} N^* &= \frac{\eta_s^*}{R_m \eta_1} \\ Y &= \frac{\eta_1}{\eta_2} \end{aligned}$$

Now, we change to logarithmic spatial variables, taking care to avoid values in the interval $[0, 1)$ inside the logarithm. Hence, we choose the change of variables

$$\begin{aligned} p &= \log(\bar{r} + 1) \\ s_1 &= \log(\bar{z} + 1), \quad (\textit{lower phase}) \\ s_2 &= \log(1 - \bar{z}), \quad (\textit{upper phase}) \end{aligned}$$

with domains

$$\begin{aligned} 0 \leq p \leq \log(\bar{R} + 1) \\ 0 \leq s_1 \leq \log(\bar{h} + 1) \\ 0 \leq s_2 \leq \log(1 + \bar{h}) \end{aligned}$$

Performing the change of variables $g_1^* = g_1^*(p, s_1)$, $g_2^* = g_2^*(p, s_2)$, the Navier-Stokes equations for both bulk phases are

$$
\begin{aligned}
iRe_1 g_1^* = {} & \frac{1}{e^{2p}}\left(\frac{\partial^2 g_1^*}{\partial p^2} - \frac{\partial g_1^*}{\partial p}\right) + \frac{1}{e^{2p}-e^p}\frac{\partial g_1^*}{\partial p} - \frac{g_1^*}{e^{2p}-2e^p+1} \\
& + \frac{1}{e^{2s_1}}\left(\frac{\partial^2 g_1^*}{\partial s_1^2} - \frac{\partial g_1^*}{\partial s_1}\right) \qquad (68) \\
iRe_2 g_2^* = {} & \frac{1}{e^{2p}}\left(\frac{\partial^2 g_2^*}{\partial p^2} - \frac{\partial g_2^*}{\partial p}\right) + \frac{1}{e^{2p}-e^p}\frac{\partial g_2^*}{\partial p} - \frac{g_2^*}{e^{2p}-2e^p+1} \\
& + \frac{1}{e^{2s_2}}\left(\frac{\partial^2 g_2^*}{\partial s_2^2} - \frac{\partial g_2^*}{\partial s_2}\right) \qquad (69)
\end{aligned}
$$

and the boundary conditions turn to

$$
\begin{aligned}
& g_j^*(0, s_j) = 0, && (70) \\
& g_1^*(p, s_1) = \log(\bar{h}+1)) = 0, && (71) \\
& g_j^*(\log(\bar{R}+1), s_j) = 0, && (72) \\
& g_j^*(0 \le p \le \log(2), 0) = e^p - 1, && (73)
\end{aligned}
$$

where equation (70) imposes symmetry of the velocity field at the rotation axis, equations (71) and (72) stand for the no-slip condition at the cup floor and lateral walls, and equation (73) represents the velocity of the fluid in contact with the probe.

Another boundary condition is required at the top surface of the upper bulk phase. Two distinct cases may be considered; either a free upper interface, i.e.,

$$
\left.\left(\frac{\partial g^*}{\partial s_2}\right)\right|_{p, s_2=\log(\bar{h}+1)} = 0, \qquad (74)
$$

or a rigid wall (no-slip) condition, namely

$$
g^*(p, s_2 = \log(\bar{h}+1)) = 0, \qquad (75)
$$

while the Boussinesq-Scriven boundary condition at the interface turns to

$$N^* \left[\frac{1}{e^{2p}} \left(\frac{\partial^2 g_s^*}{\partial p^2} - \frac{\partial g_s^*}{\partial p} \right) + \frac{1}{e^{2p} - e^p} \frac{\partial g_s^*}{\partial p} - \frac{g_s^*}{e^{2p} - 2e^p + 1} \right] = -\frac{1}{Y} \frac{\partial g_2^*}{\partial s_2} - \frac{\partial g_1^*}{\partial s_1}, \tag{76}$$

at $s_1, s_2 = 0$, $\log(2) \leq p \leq \log(\bar{R}+1)$. Notice that in the boundary condition at the interface there is no an explicit appearance of $1/e^s$ because at $s = 0$, $1/e^s = 1$. Now, the complex Boussinesq number does not appear explicitly in the expression of the Boussinesq-Scriven condition, but the proper definition [74] is $Bo^* = \frac{\eta_s^*}{R_m(\eta_1+\eta_1)}$.

Conversely, the expression for the drag torque imposed by the lower bulk phase at the lower disk surface is

$$M_1^* = i\omega 2\pi R_m^3 \eta_1 \theta_0^* e^{i\omega t} \int_0^{\log(2)} e^p (e^p - 1)^2 \left. \frac{\partial g_1^*}{\partial s_1} \right|_{s_1=0} dp, \tag{77}$$

while the corresponding expression for the drag torque imposed by the upper bulk phase at the upper disk surface is:

$$M_2^* = -i\omega 2\pi R_m^3 \eta_2 \theta_0^* e^{i\omega t} \int_0^{\log(2)} e^p (e^p - 1)^2 \left. \frac{\partial g_2^*}{\partial s_2} \right|_{s_2=0} dp. \tag{78}$$

The interfacial drag along the contact line between the microbutton and the interface is:

$$M_s^* = i\omega 2\pi R_m^3 (\eta_1 + \eta_2) Bo^* \theta_0 e^{i\omega t} \left(\frac{1}{2} \left. \frac{\partial g_s^*}{\partial p} \right|_{p=\log(2), s=0} - 1 \right), \tag{79}$$

and the complex amplitude ratio between the total torque and the microbutton angular position is:

$$\begin{aligned} AR^* = \frac{M_0^*}{\theta_0} =& i\omega 2\pi R_m^3 \left[-\eta_1 \int_0^{\log(2)} e^p (e^p - 1)^2 \left. \frac{\partial g_1^*}{\partial s_1} \right|_{s_1=0} dp \right. \\ & + \eta_2 \int_0^{\log(2)} e^p (e^p - 1)^2 \left. \frac{\partial g_2^*}{\partial s_2} \right|_{s_2=0} dp \\ & \left. -(\eta_1 + \eta_2) Bo^* \left(\frac{1}{2} \left. \frac{\partial g_s^*}{\partial p} \right|_{p=\log(2), s=0} - 1 \right) \right] - I\omega^2, \end{aligned} \tag{80}$$

where, again, the contributions from the interface and both bulk phases are easily recognized. Solving for the complex Boussinesq number, Bo^*, we can set up the following iterative scheme:

$$[Bo^*]_{k+1} = -\frac{AR^*_{exp} + i\omega 2\pi R_m^3 \left(\eta_1 \left[\bar{M}_1^*\right]_k - \eta_2 \left[\bar{M}_2^*\right]_k\right) + I\omega^2}{i\omega 2\pi(\eta_1 + \eta_2) R_m^3 \left[\bar{M}_s^*\right]_k}, \tag{81}$$

where

$$\begin{aligned}
\left[\bar{M}_1^*\right]_k &= \int_0^{\log(2)} e^p (e^p - 1)^2 \left.\frac{\partial \left[g_1^*\right]_k}{\partial s_1}\right|_{s_1=0} dp, \\
\left[\bar{M}_2^*\right]_k &= \int_0^{\log(2)} e^p (e^p - 1)^2 \left.\frac{\partial \left[g_2^*\right]_k}{\partial s_2}\right|_{s_2=0} dp, \\
\left[\bar{M}_s^*\right]_k &= \left(\frac{1}{2} \left.\frac{\partial \left[g_s^*\right]_k}{\partial p}\right|_{p=\log(2), s=0} - 1\right).
\end{aligned} \tag{82}$$

Now we will briefly illustrate the performance of this scheme by showing some preliminary results obtained for the case of a microbutton with radius $R_m = 10\,\mu$m, in a cup with radius $R_c = 2.5$ mm, with a water lower bulk phase depth $H_1 = 2.5$ mm, and a forcing frequency $\omega = \pi$ rad/s. Such values are typical of the experimental realizations [23, 24, 25, 26].

First we show the results of some convergence tests performed on the fluid mechanics computations by varying the spatial resolution (mesh spacing). The results using different rectangular meshes (in the logarithmic coordinates) with N nodes in, both, the p and s coordinates, respectively, are shown in Figure 11. The values of N must be chosen so that the node at the microbutton rim is as close as possible to the radial coordinate value $p = \log(2)$.

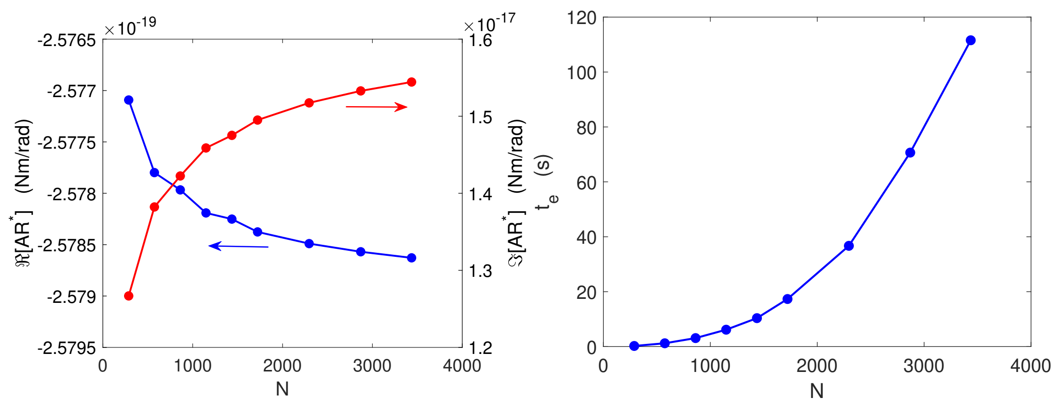

Figure 11: Left panel: Convergence of the real (blue trace) and imaginary (red trace) parts of the amplitude ratio as a function of mesh size for a clean interface ($Bo^* = 0$). Right panel: time needed to solve the hydrodynamic problem to obtain the flow field configuration as a function of mesh size.

In the left panel we show the variation of the real and imaginary parts of the complex amplitude ratio, AR^*, for a clean interface ($Bo^* = 0$) as a function of mesh size. Both components converge nicely, the convergence error being higher in $\Im[AR^*]$. The right panel of Figure 11 shows the time needed to solve the full flow field configuration as a function of the mesh size (in a desktop computer having a Pentium Core i5-4460 microprocessor and 16 Gb RAM). The computation time grows approximately with N^2. Based on the results shown in Figure 11 we have taken $N = 1722$ for the rest of the results shown here because it offers a good compromise between spatial resolution and computational time cost ($\sim$ 17.33 s for each full flow field configuration).

In Figures 12 and 13 we show color coded plots of the real and imaginary parts of the velocity amplitude function ($\Re[g_1^*(r,z)]$ and $\Im[g_1^*(r,z)]$, respectively) for different interfacial properties. Figure 12 shows the results for a clean interface, i.e., $\eta_s^* = 0$, while Figure 13 corresponds to the case $\eta_s^* = 10^{-5}$ Ns/m. Representations in both actual spatial and logarithmic coordinates (top and bottom rows, respectively) are provided. Notice that the values of $\Re[g_1^*(r,z)]$ are very small everywhere but in a very small neighborhood of the microbutton, which in the real space coordinates is located at the top left corner of the images. Consequently, we have chosen to show $\Re[g_1^*(r,z)]$ in a logarithmic colour scale.

As expected, only the real part of the velocity amplitude function takes large values (the imaginary part is everywhere three orders of magnitude smaller that the real one) and it does so close to the microbutton disk. Hence, large velocity gradients occur close to the probe. The effect of the interfacial viscosity can be clearly appreciated by the much larger radial extension of the flow close to the interface.

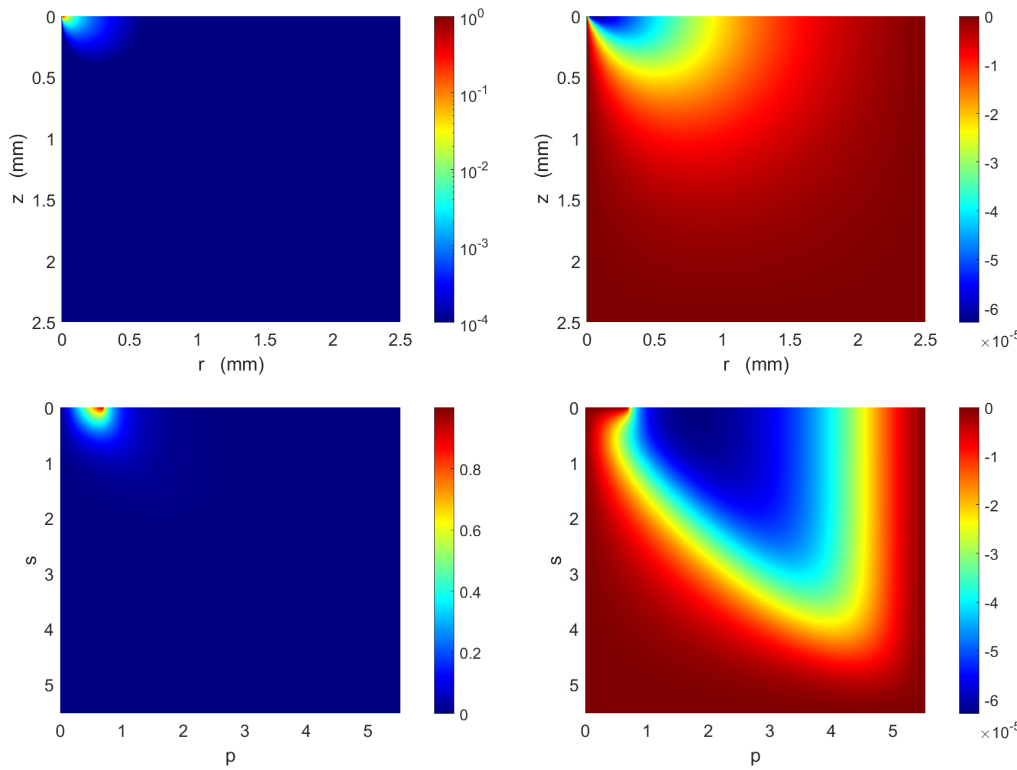

Figure 12: Color coded plots of the real and imaginary parts (left and right panels, respectively) of the velocity amplitude function, g_1^*, for the microbutton configuration indicated in the text with a clean interface ($\eta_s^* = 0$). Representation in real coordinates (top row) and logarithmic coordinates (bottom row). Notice the logarithmic color scale in the upper left panel.

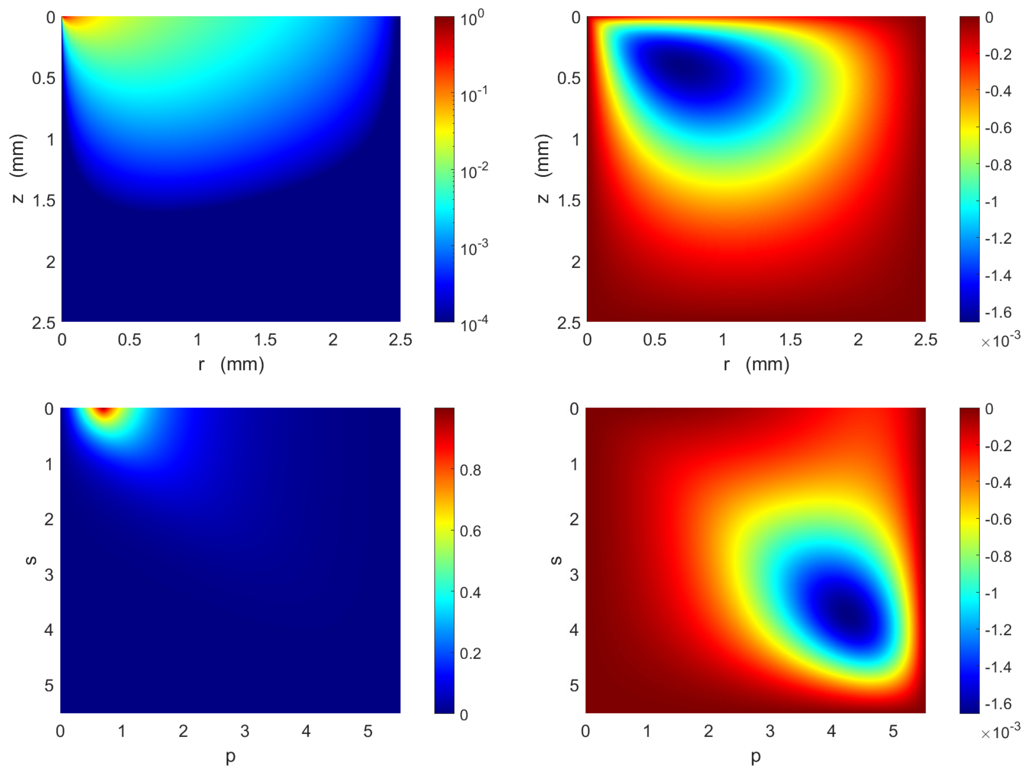

Figure 13: Color coded plots of the real and imaginary parts (left and right panels, respectively) of the velocity amplitude function, g_1^*, for the microbutton configuration indicated in the text for a purely viscous interface with $\eta_s = 10^{-5}$ Ns/m. Representation in real coordinates (top row) and logarithmic coordinates (bottom row). Notice the logarithmic color scale in the upper left panel.

In Figure 14 we show the dependence of the interfacial velocity profile, $g_s^*(r) = g^*(r, 0)$, or $g_s^*(p) = g^*(p, 0)$, on the interfacial viscosity, η_s^*, for the microbutton configuration previously indicated, at a forcing frequency $\omega = \pi$ rad/s. Results for purely viscous interfaces with $\eta_s^* = 0,\ 10^{-9},\ 10^{-7},\ 10^{-5}$, and ∞ Ns/m (green, magenta, blue, black, and brown lines, respectively), which correspond to the complex Boussinesq number values $Bo^* = \eta_s^*/(R_m \eta_1) = 0,\ 10^{-1},\ 10,\ 10^3$, and ∞, are shown. The analytical solution corresponding to $|Bo^*| \to \infty$ is obtained by considering an interface fully decoupled from the subphase, i.e., neglecting the bulk contribution to the interfacial shear stress balance (right hand side in expression (67)). The Reynolds number value is in all cases $Re_1 = 3 \times 10^{-4}$. The real, $\Re[g_s^*(r)]$, and imaginary, $\Im[g_s^*(r)]$, parts of the interfacial velocity amplitude function are shown as continuous and dotted lines, respectively. The left panel shows the plots in the real space coordinate r, while the right panel shows the plot of $|\Re[g_s^*(p)]|$ as a function of the logarithmic variable p and with a logarithmic scale in the corresponding vertical axis.

In all of the cases, $\Re[g_s^*(r)]$ is a rapidly decreasing function of r, which for low values of Bo^* changes sign (see the downward peak in the green and magenta traces at the right panel) at a logarithmic radial position $p \sim 5.2$, i.e., $r \sim 1.8$ mm. As expected, increasing the interfacial viscosity, η_s^*, increases the distance in which $\Re[g_s^*(r)]$ decays and, consequently, the curves tend to show a less steep decay. For values of the complex Boussinesq number $Bo^* \geq 10^3$ the curves corresponding to $\Re[g_s^*(r)]$ are not distinguishable from each other and they decrease in the whole range of the radial coordinate.

$\Im[g_s^*(r)]$ always shows negative values, typically much smaller in modulus that those pertaining to $\Re[g_s^*(r)]$. However, the variation of $\Im[g_s^*(r)]$ with the interfacial viscosity is not monotonous. Actually, starting from $\eta_s^* = 0$, the modulus of $\Im[g_s^*(r)]$ increases with η_s^* up to some value of about 10^{-7} Ns/m, above which the modulus of $\Im[g_s^*(r)]$ starts decreasing because in the limit of very high interfacial viscosity (i.e., $l_\omega^s >> R_c$) the imaginary part of the velocity amplitude function vanishes, as shown in the right panel of Figure 14.

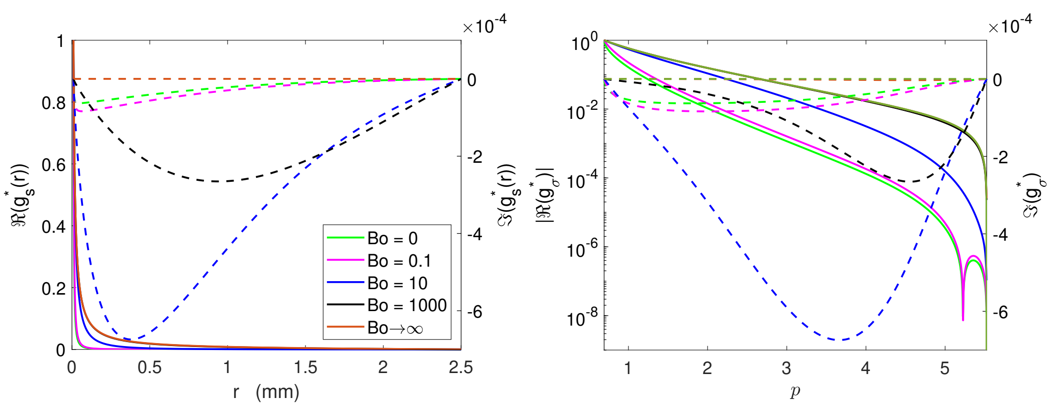

Figure 14: Radial plots of the real and imaginary parts (continuous and dotted lines, respectively) of the velocity amplitude function, g_s^* at the interface, for viscous interfaces with $\eta_s^* = 0$, 10^{-9}, 10^{-7}, 10^{-5} and ∞ Ns/m (light green, magenta, blue, black, and dark green lines, respectively), represented in the real space coordinate, r. Left and right panels show $g_s^*(r)$ and $g_s^*(p)$ values, respectively. Notice that in the right panel the vertical scale of the left vertical axis is logarithmic. The legend in the left panel applies to the right panel too.

In order to study the consistency of the iterative scheme [38], [39] to obtain the converged value of the complex Boussinesq number and, consequently the value of η_s^*, we have performed the same two step process described in the bicone section of this report, i.e., i) solving the fluid dynamical problem for different values of the complex interfacial viscosity and computing the corresponding amplitude ratio, AR^*, and ii) feeding the iterative process with the AR^* values found in order to obtain the converged value of the complex Boussinesq number and, consequently, the converged value of η_s^*. All computations have been made on the same system geometry considered up to here and at the same frequency.

We have applied such a procedure to interfaces that are purely viscous, with $\eta_s^* = \eta_s$, viscoelastic, with $\eta_s' = \eta_s'' = \eta_s$ (i.e., $\eta_s^* = (1-i)\eta_s$), and purely elastic, with $\eta_s^* = -i\eta_s$. The values of η_s have spanned the range $10^{-13} \leq \eta_s \leq 10^{-5}$ Ns/m and we have recorded the corresponding number of iterations needed to attain convergence. The results are represented in Figure 15, where the left panels show the values of the real and imaginary parts of η_s^* obtained after convergence, namely $[\eta_s']_c$ (filled symbols) and $[\eta_s'']_c$ (open symbols), as a function of the programmed value of η_s. The red line represents the perfect consistency line, $[\eta_s']_c = [\eta_s'']_c = |\eta_s|$. Top, middle, and bottom panels correspond, respectively, to the cases of purely viscous, viscoelastic, and purely elastic interfaces. The right panels in Figure 15 indicate, in each case, the number of iterations needed for convergence of the iterative process.

For the purely viscous interfaces (top row), the value of η_s' is nicely recovered, while numerical errors yield a value of η_s'' that is always at least six orders of magnitude smaller than the value of η_s'. For the viscoelastic interfaces (middle row), both the real and imaginary parts of the complex interfacial viscosity are nicely recovered by the iterative process. For the purely elastic interfaces (bottom row), the value of η_s'' is nicely recovered, while numerical errors yield a value of η_s' that is always at least three orders of magnitude smaller than the value of η_s'. The plots of the number of iterations needed for convergence are very similar to each other in the three cases considered, varying between 5 and 25 iterations in the full complex viscosity range here studied. A full report of the numerical study will be given in a separate publication. According to the results shown here, the microbutton ISR appears to be an excellent candidate for the application of the flow field-based data analysis techniques here described.

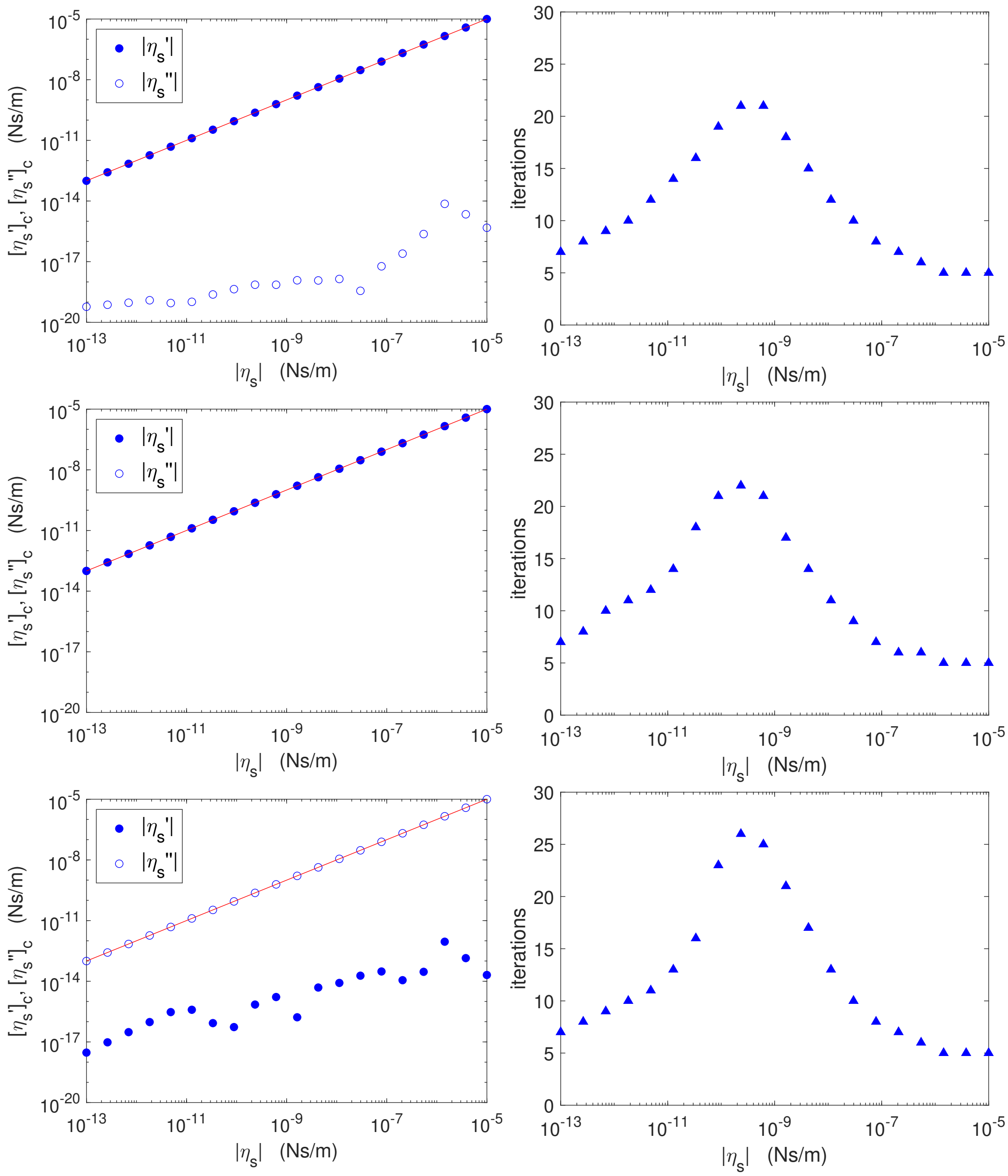

Figure 15: Results of the consistency test, for $R_m = 10$ μm and $\omega = \pi$ rad/s, for purely viscous (top row), viscoelastic (middle row), and purely elastic (bottom row) interfaces with real and imaginary parts of the complex interfacial viscosity in the range $10^{-13} < \eta_s < 10^{-5}$ Ns/m. Left panels: Comparison of the converged values $[\eta_s']_c$ (filled symbols), and $[\eta_s'']_c$ with the programmed value η_s (red line). Right panels: Number of iterations needed for convergence for the results in the corresponding left panel.

6.2. Extension to 3D rheometry

As shown in the previous Sections of this report, the application of flow field-based data analysis techniques has i) extended the usability window of interfacial shear rheometers, ii) allowed for a much better separation of the viscous and elastic components of the response, and iii) considerably improved our understanding of the flow field dynamics in the main practical interfacial rheometer configurations. Would there be any gain in transposing such techniques to bulk rheometry? The answer is most probably yes in situations were the structure of the flow field departs from the linear velocity profile configuration at the subphase or the interface. For instance, two aspects in which the application of FFBDA techniques in bulk rheology are expected to be advantageous are the study of very soft samples (water-like viscosity), where the structure of the flow field would easily develop a nonlinear vertical velocity profile, and shear banding problems where the combination of a shear thinning constitutive equation with fluid inertia would easily produce a low viscosity highly sheared region close to the moving probe.

In the context of bulk rheology we will use the terms "gap loading" and "surface loading" [8], most used when dealing with the plate-plate configuration in rotational bulk rheometry, as corresponding to the two limiting cases regarding the flow field configuration: "gap loading" refers to the case where fluid inertia is negligible (typically, very small gap and low frequency) and the vertical velocity profile is linear, while surface loading refers to the case where fluid inertia is relevant (typically, at large gaps and/or high frequency) and the vertical velocity profile is nonlinear.

To our knowledge, all commercial rheometers process the torque and angular displacement experimental data with simple expressions that are correct exclusively for the gap loading situation, i.e., for linear vertical velocity profiles. As soon as the experimental situation deviates from the gap loading situation, the values output by the rheometer software are in error, while flow field-based techniques may deal with the nonlinear vertical velocity profile easily, yielding more accurate values of the dynamic moduli, with a more realistic separation of elastic and viscous components.

Among the many possibilities that can be thought as extensions of the techniques previously described we will like to mention three combinations of experimental systems with already published FFBDA software that require minimum or null software development:

i) Suitably adapting the flat plate approximation scheme here shown for the bicone bob to the analysis of experimental data obtained in the plate-plate configuration in bulk rheometry. Here $Bo^* = 0$ and the iterative process should be organized around the Reynolds number, i.e., the probe equation of motion will have a single drag torque, corresponding to the lower bulk phase. Solving the equation of motion for Re (or the bulk phase viscosity) will give the expression on which to build the iterative process. Such a procedure will certainly extend the usability window in the cases where the "gap loading" condition is not fulfilled anymore because the Stokes length scale becomes smaller than the plate-plate gap in an upwards frequency sweep.

ii) Using the bicone configuration with a lower bulk subphase and an interfacial film with known interfacial viscosity. Choosing a fluid with a low viscosity and low vapor pressure for the interfacial film, and setting an adequate film depth, one might have an interfacial film with known interfacial viscosity and impermeable to the bulk phase solvent. Here the probe equation of motion will have both bulk phase and interfacial contributions to the drag torques. Solving, then, the probe equation of motion for the bulk phase viscosity will provide the expression for the iterative process. Such a system will be adequate for rheological studies of low viscosity bulk samples with high vapor pressure.

iii) Using the high sensitivity instruments and data analysis schemes developed for interfacial rheology (DWR, magnetic tweezers, or microbutton ISRs) to measure the rheological properties of bulk samples with or without interfacial layers. Here again, the probe equation of motion should be solved for the Reynolds number or the bulk phase viscosity to set up the iterative scheme. In the following we will illustrate the application of this last scheme to measure the viscosity of water/glycerol mixtures with, both, the magnetic tweezers and the bicone ISR.

Solutions of glycerol (Merck, Reagent grade) in Milli-Q quality water were prepared at percent volume concentrations that were multiples of 10. The solutions were freshly prepared, sonicated for 15-20 minutes, and stored for at least 24 hours at room temperature before use. The samples were put in a 3D-printed PLA block with an excavated pool consisting in a concavity shaped as a horizontal half cylinder (100 mm long and 16 mm in diameter) connected by a small channel to a 40×40 mm square pool (with a depth of 4 mm), that is used to measure the interface temperature by means of a pyrometer. The cavity is filled up to the pool rim always with the same sample volume so that good horizontality of the interface and the same vertical distance between the magnets and the needle are assured. The sample temperature was controlled to within $\pm 0.05^o$C, by placing the 3D-printed block on top of a much larger Aluminum plate thermostated by means of a temperature controlled circulation bath (Polyscience 9110) with ± 0.01°C precision. A pyrometer (Micro-Epsilon CS-micro-2W) having ± 25 mK resolution was used to measure the interfacial temperature continuously.

The magnetic tweezers ISR, together with the probe calibration procedure, has been fully described in reference [27] for both the microwires [28] and the commercial needles. Here, two different microwires were used, with diameter $a = 24.6$ μm, lengths of 8.5 and 9.0 mm, and masses of 19.5 and 20.6 μg, respectively.

The measurements were performed by imposing an oscillatory displacement of amplitude $z_0 = 200\,\mu$m and frequency $\omega = \pi$ rad/s on the magnetic trap. The large viscosity measurements were made with a vertical distance $h = 20$ mm between the probe and the magnet trap, while the small viscosity measurements were made with $h = 35$ mm. For each sample, 20 independent experiments with a typical time span of 10-15 periods of the forcing signal were performed.

As stated above, the data analysis procedure is identical to the interfacial rheology one, with the only exception that the iterative scheme has to be changed. In this case, no interfacial film is present, so that the Boussinesq-Scriven boundary condition, equation (16), must be substituted by the free surface boundary condition (null vertical velocity gradient at the interface). Moreover, the term corresponding to the interfacial drag torque in the probe equation of motion can be dropped and, upon solving for Re^*, the following iterative scheme can be proposed:

$$[Re^*]_{k+1} = \frac{i2L\omega^2 a^2 \rho \int_0^{\pi/2} \left(-\partial [g^*]_k/\partial p)\right|_{p=0} d\theta}{(AR^*_{exp} - 1)k_{mt} + m\omega^2}, \tag{83}$$

where ρ and m are the bulk fluid density and the rod mass, respectively.

For each sample, we performed a set of 20 measurements at a fixed frequency $\omega = \pi$ rad/s. The results of such measurements are shown in Figure 16, where the left and right panels show, respectively, a typical example of a set of 20 measurements at fixed frequency and the global results for all of the measurements made at different concentrations.

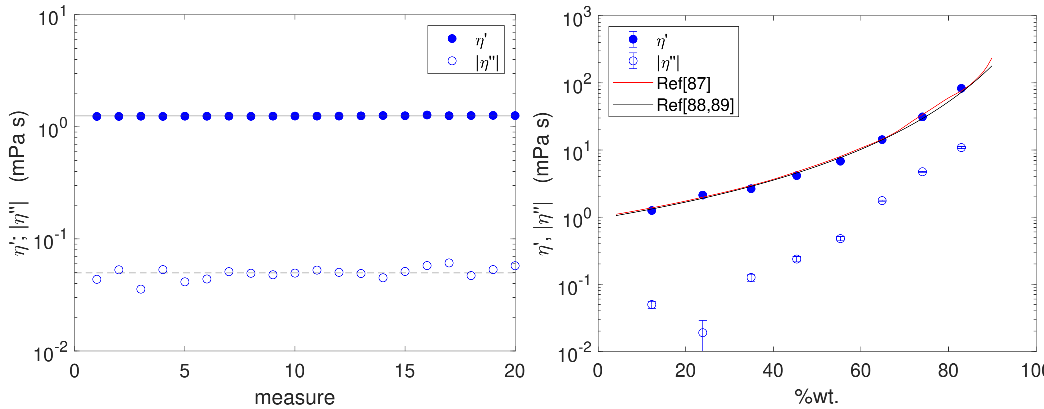

Figure 16: Bulk rheology measurements with the magnetic rod ISR on glycerol in water solutions. Left panel: Set of 20 measurements at $C = 12.25$ %wt. and $\omega = \pi$ rad/s (filled symbols: η'; open symbols: η''). Right panel: η' and η'' versus concentration (filled symbols: η'; open symbols: η''; red line: reference data [87]; black line: data computed with the van de Ven equation [88, 89]).

The left panel in Figure 16 shows a typical example of a sequence of the 20 values obtained for η' and $|\eta''|$, just to give an idea of the variability of the individual measurements. In this case the data correspond to a sample with 10%vol. = 12.3%wt. concentration, at a temperature $T = 22.3 \pm 0.6^o C$. For this particular case, the individual measurements are dispersed in the $1.24 \leq \eta' \leq 1.28$ mPas interval, the average value is $\bar{\eta'} = 1.25$ mPas, and the standard deviation is 0.01 mPas. The results obtained for all of the concentration values explored are shown in the left panel, together with the reference data, according to [87], and data computed from the van de Ven equation [88, 89]. The error bars of the experimental results are typically smaller than the symbol size. The agreement of the results here obtained with the reference and numerical data is remarkable.

An equivalent scheme can be devised for the bicone ISR by discarding the M^*_{surf} term in equation (53) and solving it for the complex Reynolds number, so that the following iterative scheme is obtained:

$$[Re^*]_{k+1} = \frac{i\omega^2 2\pi\rho R_b R_c^2 \int_0^{R_b} r^2 \left(\frac{\partial [g^*]_k}{\partial z}\right)\Big|_{z=h} dr}{AR_{exp} + I\omega^2 - ib\omega}. \tag{84}$$

The very same aforementioned glycerol in water solutions were used in the experiments made with the bicone ISR, in the configuration shown in Figure

1c, whose physical parameters were described in detail in [37], mounted on a Bohlin C-VOR rheometer. In the measurements reported here, the sample depth was $h = 10$ mm. For each sample, 20 to 25 independent experiments with a typical time span of 4 periods of the forcing signal were performed. The angular displacement signals showed important drifts for the low viscosity cases; before applying the FFBDA scheme the drift was subtracted.

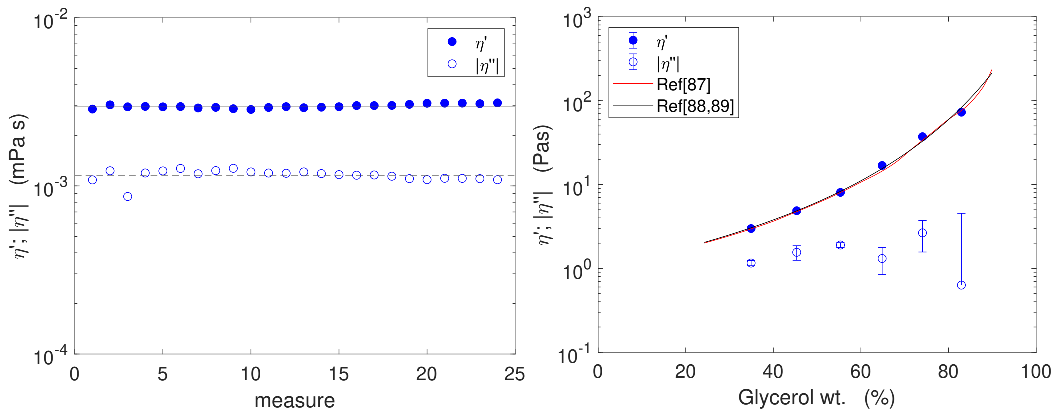

Figure 17: Bulk rheology measurements with the bicone ISR on glycerol in water solutions. Left panel: Set of 25 measurements at $C = 34.9$ %wt. and $\omega = 10\pi$ rad/s (filled symbols: η'; open symbols: η''; lines represent average values). Right panel: η' and η'' versus concentration (filled symbols: η'; open symbols: η''; red line: reference data [87]; black line: data computed with the van de Ven equation [88, 89]).

The left panel in Figure 17 shows a typical example of a sequence of the 20 values obtained for η' and $|\eta''|$. In this case the data correspond to a sample with 30%vol. = 34.93%wt. concentration, at a temperature $T = 20.0 \pm 0.1^oC$. For this particular case, the individual measurements are dispersed in the $2.85 \leq \eta' \leq 3.12$ mPas interval, the average value is $\bar{\eta'} = 2.85$ mPas, and the standard deviation is 0.12 mPas. Although the individual measurements have a slightly larger variability than those obtained with the microwire ISR, the agreement of the global results with the reference data [87], and data computed from the van de Ven equation [88, 89] is, again, remarkable.

Such a precision is hardly achievable with the C-VOR in the regular plate-plate configuration even at very small gap size. Moreover, the range of validity of the standard rheometer software for data processing, that is strictly applicable only for the case of linear vertical velocity profile, will be limited in frequency. For instance, for a water sample and a 500 μm gap, the vertical velocity profile will be nonlinear for $f \geq \frac{\eta}{2\pi\rho H_1^2} \sim 0.6$ Hz, and the values output by the rheometer will be in error.

Interestingly, when using instruments designed for interfacial rheology to make bulk rheological measurements the disadvantage of the bicone ISR, with respect to the DWR or the MNISR, is compensated to a certain extent. Obviously, the larger area of contact of the bicone surface with the bulk sample is not anymore a shortcoming because it increases, comparatively, the drag torque sensed by the probe. Anyway, the fact that viscosities of a few mPas can be accurately measured with a sample 10 mm deep gives a good idea of the gain attainable with the use of FFBDA methods in bulk rheology.

7. Conclusions and final comments

In this report we have presented a unified view of the different flow field-based interfacial rheology data analysis schemes publicised up to date. The initial development of such schemes for the MNISR or the DWR are already about a decade old [35, 22, 36] and are at work in many interfacial rheology laboratories. The development of such schemes for the bicone bob rotational ISR is much more recent [37, 38, 39]. Interestingly, some commercial builders of rotational interfacial rheometers already offer data analysis software packages incorporating flow field-based data analysis.

A first conclusion can be drawn directly from the comparative performance tests made on the MNISR and the bicone ISR in Section 2: flow field-based data analysis techniques have the potential to cope with nonlinear velocity profiles both at the interface and in the surrounding bulk phases. Such nonlinear velocity profiles pervade the practical situations in interfacial rheometry for moderate to low values of the complex Boussinesq number, Bo^*, where the flow field-based data analysis methods yield not only more realistic values of the sample's rheological properties but also the structure of the flow field within the sample. This allows for a much better knowledge and assessment of the experimental conditions, a more realistic separation of interfacial and bulk contributions, and a more precise separation of the elastic and viscous components of the sample's response. On the other hand, the techniques here described require data analysis procedures that are more complex, mathematically and numerically, and at significantly larger computational (memory and time) cost. However, we have also shown that the spatial resolution and computation times are manageable with nowadays desktop personal computers, so that embedding flow field-based techniques in the real time control and measurement software of commercial or "home-made" rheometers is currently feasible.

Moreover, we have provided examples of the possibility to extend the application of flow field-based techniques to two other cases: i) the data analysis of the measurements performed with the micro-button ISR, which requires some particular considerations because of the great disparity between the micro-button and cup sizes, and ii) the application of such techniques in the 3D rheometry of soft bulk samples, which we exemplify through the analysis of bulk rheometry experimental data obtained in the MNISR and the bicone bob ISR on glycerol in water solutions. The results of both new examples appear to be very promising. Applying such techniques to bulk rheology of soft samples (water-like viscosity samples) is particularly appealing because in such situations the bulk viscous length scale will be typically very small and the application of the classical data analysis based on very simple flow configurations may yield significant errors, while flow field-based techniques may deal with the nonlinear flow field configurations rather easily.

A key point in the understanding of the origin and the consequences of the existence of the nonlinear velocity profiles is the role of the viscous length scales [46], both at the interface, ℓ^s_ω, and the bulk subphase, ℓ_ω, and their competition with the lateral extension of the interface, $R_c - R_b$, and the depth, H_1, of the bulk subphase. Such concepts have been used, for instance, in discussing the subphase flow structure in the bicone case, and can be used with benefit in other instruments as, for instance, the rotational rheometers working in controlled strain mode.

Some caveats are in order here, however. Obviously, the limitations of the particular physical model chosen for a given geometry are imported directly into the data analysis scheme. For instance, in all geometries here considered, very simple flow field configurations have been used, having only one non null and highly symmetric component of the velocity. Situations in which those two conditions are not fulfilled cannot be dealt with, evidently. Additionally, the rheological properties of the sample are assumed to be dependent only on frequency, but not on the local deformation or shear rate. Hence, problems involving spatially non uniform rheological properties are out of the scope of the techniques here described. Nonetheless, it is conceivable that some simple constitutive equations supplemented with a suitable definition of the local shear rate might be incorporated into the formulation of the fluid mechanical problem. From the mathematical point of view, the main open front is that, to our knowledge, there is not a theorem stating that the iterative process has a single stable fixed point. In fact, although rare, some consistency problems may appear, as we have shown in the case of purely elastic interfaces. Hence, the results obtained when applying the procedures here described have to be analyzed with care.

Acknowledgements

The authors acknowledge partial support from MINECO (Grant No. FIS2017-86007-C3-3-P). P.S.P. acknowledges the Programa Operativo Empleo Juvenil, co-funded by the Fondo Social Europeo and the Ministerio de Ciencia e Innovación (MICINN) and UNED for the funding of the contract with reference No. PEJ2018-005480-A.

References

[1] R. Bird, C. Curtiss, R. Armstrong, O. Hassager, Dynamics of Polymeric Liquids, Volume 1: Fluid Mechanics, 2nd ed., John Wiley & Sons, 1987.

[2] C. W. Macosko, Rheology Principles, Measurements and Applications, VCH Publishers, 1994. URL: https://ci.nii.ac.jp/naid/10005741026/en/.

[3] R. G. Larson, The Structure and Rheology of Complex Fluids, Oxford University Press, 1999.

[4] R. I. Tanner, Enginneering Rheology, 2nd ed., Oxford University Press, 2010.

[5] N. Phan Tien, N. Mai-Duy, Understanding Viscoelasticity, 3rd ed., Springer, 2017.

[6] J. Dealy, D. J. Read, R. G. Larson, Structure and Rheology of Molten Polymers, 2nd ed., Hanser Publishers, 2018.

[7] I. M. Krieger, Bingham Award Lecture—1989: The role of instrument inertia in controlled-stress rheometers, Journal of Rheology 34 (1990) 471–483. URL: http://sor.scitation.org/doi/10.1122/1.550138. doi:10.1122/1.550138.

[8] J. L. Schrag, Deviation of velocity gradient profiles from the "gap loading" and "surface loading" limits in dynamic simple shear experiments, Transactions of the Society of Rheology 21 (1977) 399–413. doi:10.1122/1.549445.

[9] T. E. R. Jones, J. M. Davies, A. Thomas, Fluid inertia effects on a Controlled Stress Rheometer in its oscillatory mode, Rheologica Acta 26 (1987) 14–19. URL: http://link.springer.com/10.1007/BF01332679. doi:10.1007/BF01332679.

[10] C. Baravian, G. Benbelkacem, F. Caton, Unsteady rheometry: can we characterize weak gels with a controlled stress rheometer?, Rheologica Acta 46 (2007) 577–581. URL: http://link.springer.com/10.1007/s00397-006-0135-x. doi:10.1007/s00397-006-0135-x.

[11] J. Läuger, H. Stettin, Effects of instrument and fluid inertia in oscillatory shear in rotational rheometers, Journal of Rheology 60 (2016) 393–406. URL: https://doi.org/10.1122/1.4944512. doi:10.1122/1.4944512. arXiv:https://doi.org/10.1122/1.4944512.

[12] R. H. Ewoldt, M. T. Johnston, L. M. Caretta, Experimental challenges of shear rheology: How to avoid bad data, in: S. E. Spagnolie (Ed.), Complex Fluids in Biological Systems: Experiment, Theory, and Computation, Springer New York, New York, NY, 2015, pp. 207–241. URL: https://doi.org/10.1007/978-1-4939-2065-5_6. doi:10.1007/978-1-4939-2065-5_6.

[13] J. C.-W. Lee, Y.-T. Hong, K. M. Weigandt, E. G. Kelley, H. Kong, S. A. Rogers, Strain shifts under stress-controlled oscillatory shearing in theoretical, experimental, and structural perspectives: Application to probing zero-shear viscosity, Journal of Rheology 63 (2019) 863–881. URL: https://doi.org/10.1122/1.5111358. doi:10.1122/1.5111358. arXiv:https://doi.org/10.1122/1.5111358.

[14] O. Hassager, Stress-controlled oscillatory flow initiated at time zero: A linear viscoelastic analysis, Journal of Rheology 64 (2020) 545–550. URL: https://doi.org/10.1122/1.5127827. doi:10.1122/1.5127827. arXiv:https://doi.org/10.1122/1.5127827.

[15] D. A. Edwards, H. Brenner, D. T. Wasan, A. M. Kraynik, Interfacial Transport Processes and Rheology, Butterworth-Heinemann, Boston, 1991. URL: https://www.elsevier.com/books/interfacial-transport-processes-and-rheology/brenner/978-0-7506-9185-7.

[16] R. Miller, L. Liggieri, Interfacial Rheology, Progress in Colloid and Interface Science, CRC Press, 2009. URL: https://books.google.es/books?id=pT9pNObvRD8C.

[17] J. Krägel, S. Derkatch, R. Miller, Interfacial shear rheology of protein–surfactant layers, Advances in Colloid and Interface Science 144 (2008) 38–53. URL: https://www.sciencedirect.com/science/article/pii/S0001868608001243?via{%}3Dihubhttps://linkinghub.elsevier.com/retrieve/pii/S0001868608001243. doi:10.1016/j.cis.2008.08.010.

[18] G. G. Fuller, J. Vermant, Complex fluid-fluid interfaces: Rheology and structure, Annual Review of Chemical and Biomolecular Engineering 3 (2012) 519–543. URL: https://doi.org/10.1146/annurev-chembioeng-061010-114202. doi:10.1146/annurev-chembioeng-061010-114202. arXiv:https://doi.org/10.1146/annurev-chembioeng-061010-114202.

[19] M. Nagel, T. A. Tervoort, J. Vermant, From drop-shape analysis to stress-fitting elastometry, Advances in Colloid and Interface Science 247 (2017) 33 – 51. URL: http://www.sciencedirect.com/science/article/pii/S0001868617302701. doi:https://doi.org/10.1016/j.cis.2017.07.008, dominique Langevin Festschrift: Four Decades Opening Gates in Colloid and Interface Science.

[20] N. Jaensson, J. Vermant, Tensiometry and rheology of complex interfaces, Current Opinion in Colloid and Interface Science 37 (2018) 136–150. URL: https://www.scopus.com/inward/record.uri?eid=2-s2.0-85055130092&doi=10.1016%2fj.cocis.2018.09.005&partnerID=40&md5=3f7e50a95afdeac89fa5671a3496251d. doi:10.1016/j.cocis.2018.09.005, cited By 26.

[21] J. Krägel, Surface shear rheology, in: R. Miller, L. Liggieri (Eds.),

Interfacial Rheology, volume 1, CRC Press, New York, NY, 2009, pp. 372–428.

[22] S. Vandebril, A. Franck, G. G. Fuller, P. Moldenaers, J. Vermant, A double wall-ring geometry for interfacial shear rheometry, Rheologica Acta 49 (2010) 131–144. doi:10.1007/s00397-009-0407-3.

[23] Z. A. Zell, L. G. Leal, T. M. Squires, Microfabricated deflection tensiometers for insoluble surfactants, Applied Physics Letters 97 (2010) 133505. URL: http://www.pnas.org/lookup/doi/10.1073/pnas.1315991111http://aip.scitation.org/doi/10.1063/1.3491549. doi:10.1063/1.3491549.

[24] S. Q. Choi, S. G. Jang, A. J. Pascall, M. D. Dimitriou, T. Kang, C. J. Hawker, T. M. Squires, Synthesis of multifunctional micrometer-sized particles with magnetic, amphiphilic, and anisotropic properties, Advanced Materials 23 (2011) 2348–2352. doi:10.1002/adma.201003604.

[25] Z. A. Zell, A. Nowbahar, V. Mansard, L. G. Leal, S. S. Deshmukh, J. M. Mecca, C. J. Tucker, T. M. Squires, Surface shear inviscidity of soluble surfactants, Proceedings of the National Academy of Sciences 111 (2014) 3677–3682. URL: http://www.pnas.org/lookup/doi/10.1073/pnas.1315991111. doi:10.1073/pnas.1315991111.

[26] Z. A. Zell, V. Mansard, J. Wright, K. Kim, S. Q. Choi, T. M. Squires, Linear and nonlinear microrheometry of small samples and interfaces using microfabricated probes, Journal of Rheology 60 (2016) 141–159. URL: http://dx.doi.org/10.1122/1.4937931http://sor.scitation.org/doi/10.1122/1.4937931. doi:10.1122/1.4937931.

[27] J. Tajuelo, J. M. Pastor, M. A. Rubio, A magnetic rod interfacial shear rheometer driven by a mobile magnetic trap, Journal of Rheology 60 (2016) 1095–1113. URL: http://sor.scitation.org/doi/10.1122/1.4958668. doi:10.1122/1.4958668.

[28] J. Tajuelo, J. M. Pastor, F. Martínez-Pedrero, M. Vázquez, F. Ortega, R. G. Rubio, M. A. Rubio, Magnetic Microwire Probes for the Magnetic Rod Interfacial Stress Rheometer, Langmuir 31 (2015) 1410–1420. URL: http://pubs.acs.org/doi/10.1021/la5038316. doi:10.1021/la5038316.

[29] D. Dervichian, M. Joly, Transformations d'ordre supérieur dans les couches monomoléculaires, J. Phys. Radium 10 (1939) 375–384. URL: https://hal.archives-ouvertes.fr/jpa-00233687. doi:10.1051/jphysrad:01939001008037500.

[30] R. J. Myers, W. D. Harkins, The viscosity (or fluidity) of liquid or plastic monomolecular films, The Journal of Chemical Physics 5 (1937) 601–603. URL: https://doi.org/10.1063/1.1750084. doi:10.1063/1.1750084. arXiv:https://doi.org/10.1063/1.1750084.

[31] W. D. Harkins, J. G. Kirkwood, The viscosity of monolayers: Theory of the surface slit viscosimeter, The Journal of Chemical Physics 6 (1938) 53–53. URL: https://doi.org/10.1063/1.1750123. doi:10.1063/1.1750123. arXiv:https://doi.org/10.1063/1.1750123.

[32] W. D. Harkins, J. G. Kirkwood, Note on surface viscosimetry, The Journal of Chemical Physics 6 (1938) 298–298. URL: https://doi.org/10.1063/1.1750252. doi:10.1063/1.1750252. arXiv:https://doi.org/10.1063/1.1750252.

[33] G. C. Nutting, W. D. Harkins, The viscosity of monolayers: a test of the canal viscosimeter, Journal of the American Chemical Society 62 (1940) 3155–3161. URL: https://doi.org/10.1021/ja01868a073. doi:10.1021/ja01868a073. arXiv:https://doi.org/10.1021/ja01868a073.

[34] L. Scriven, Dynamics of a fluid interface Equation of motion for Newtonian surface fluids, Chemical Engineering Science 12 (1960) 98–108. URL: https://linkinghub.elsevier.com/retrieve/pii/0009250960870030. doi:10.1016/0009-2509(60)87003-0.

[35] S. Reynaert, C. F. Brooks, P. Moldenaers, J. Vermant, G. G. Fuller, Analysis of the magnetic rod interfacial stress rheometer, Journal of Rheology 52 (2008) 261–285. URL: http://sor.scitation.org/doi/10.1122/1.2798238. doi:10.1122/1.2798238.

[36] T. Verwijlen, P. Moldenaers, H. A. Stone, J. Vermant, Study of the Flow Field in the Magnetic Rod Interfacial Stress Rheometer, Langmuir 27 (2011) 9345–9358. URL: https://pubs.acs.org/doi/10.1021/la201109u. doi:10.1021/la201109u.

[37] J. Tajuelo, M. A. Rubio, J. M. Pastor, Flow field based data processing for the oscillating conical bob interfacial shear rheometer, Journal of Rheology 62 (2017) 295–311. URL: http://sor.scitation.org/doi/10.1122/1.5012764. doi:10.1122/1.5012764.

[38] P. Sánchez-Puga, J. Tajuelo, J. Pastor, M. Rubio, Dynamic Measurements with the Bicone Interfacial Shear Rheometer: Numerical Bench-Marking of Flow Field-Based Data Processing, Colloids and Interfaces 2 (2018) 69. URL: www.mdpi.com/journal/colloidshttp://www.mdpi.com/2504-5377/2/4/69. doi:10.3390/colloids2040069.

[39] P. Sánchez-Puga, J. Tajuelo, J. M. Pastor, M. A. Rubio, BiconeDrag—A data processing application for the oscillating conical bob interfacial shear rheometer, Computer Physics Communications 239 (2019) 184–196. URL: https://linkinghub.elsevier.com/retrieve/pii/S0010465519300396. doi:10.1016/j.cpc.2019.01.020.

[40] P. Saffman, M. Delbrück, Brownian motion in biological membranes, Proceedings of the National Academy of Sciences 72 (1975) 3111–3113.

[41] B. D. Hughes, B. A. Pailthorpe, L. R. White, The Translational And Rotational Drag On A Cylinder Moving In A Membrane, Journal of Fluid Mechanics 110 (1981) 349–372. doi:10.1017/S0022112081000785.

[42] K. Danov, R. Aust, F. Durst, U. Lange, Influence of the surface viscosity on the hydrodynamic resistance and surface diffusivity of a large brownian particle, Journal of colloid and interface science 175 (1995) 36–45.

[43] K. D. Danov, R. Dimova, B. Pouligny, Viscous drag of a solid sphere straddling a spherical or flat surface, Physics of Fluids 12 (2000) 2711–2722.

[44] R. Dimova, K. Danov, B. Pouligny, I. B. Ivanov, Drag of a solid particle trapped in a thin film or at an interface: influence of surface viscosity and elasticity, Journal of Colloid and Interface Science 226 (2000) 35–43.

[45] T. M. Fischer, P. Dhar, P. Heinig, The viscous drag of spheres and filaments moving in membranes or monolayers, Journal of Fluid Mechanics 558 (2006) 451.

[46] S. Fitzgibbon, E. S. G. Shaqfeh, G. G. Fuller, T. W. Walker, Scaling analysis and mathematical theory of the interfacial stress rheometer, Journal of Rheology 58 (2014) 999–1038. doi:10.1122/1.4876955.

[47] D. Renggli, A. Alicke, R. H. Ewoldt, J. Vermant, Operating windows for oscillatory interfacial shear rheology, Journal of Rheology 64 (2020) 141–160. URL: https://doi.org/10.1122/1.5130620http://sor.scitation.org/doi/10.1122/1.5130620. doi:10.1122/1.5130620.

[48] G. T. Shahin, The Stress Deformation Interfacial Rheometer, Ph.D. thesis, The University of Pennsylvania, 1986.

[49] C. F. Brooks, G. G. Fuller, C. W. Frank, C. R. Robertson, Interfacial stress rheometer to study rheological transitions in monolayers at the air-water interface, Langmuir 15 (1999) 2450–2459. doi:10.1021/la980465r.

[50] K. Yu, H. Zhang, S. Biggs, Z. Xu, O. J. Cayre, D. Harbottle, The rheology of polyvinylpyrrolidone-coated silica nanoparticles positioned at an air-aqueous interface, Journal of Colloid and Interface Science 527 (2018) 346 – 355. URL: http://www.sciencedirect.com/science/article/pii/S0021979718305502. doi:https://doi.org/10.1016/j.jcis.2018.05.035.

[51] J. Ding, H. E. Warriner, J. A. Zasadzinski, Viscosity of two-dimensional suspensions, Phys. Rev. Lett. 88 (2002) 168102. URL: https://link.aps.org/doi/10.1103/PhysRevLett.88.168102. doi:10.1103/PhysRevLett.88.168102.

[52] E. Hermans, J. Vermant, Interfacial shear rheology of dppc under physiologically relevant conditions, Soft Matter 10 (2014) 175–186. URL: http://dx.doi.org/10.1039/C3SM52091A. doi:10.1039/C3SM52091A.

[53] A. S. Luviano, J. Campos-Terán, D. Langevin, R. Castillo, G. Espinosa, Mechanical properties of dppc–pope mixed langmuir monolayers, Langmuir 35 (2019) 16734–16744. URL: https://doi.org/10.1021/acs.langmuir.9b02995. doi:10.1021/acs.langmuir.9b02995. arXiv:https://doi.org/10.1021/acs.langmuir.9b02995, pMID: 31790592.

[54] N. I. Rabiah, C. W. Scales, G. G. Fuller, The influence of protein deposition on contact lens tear film stability, Colloids and Surfaces B: Biointerfaces 180 (2019) 229 – 236. URL: http://www.sciencedirect.com/science/article/pii/S0927776519302826. doi:https://doi.org/10.1016/j.colsurfb.2019.04.051.

[55] J. Tajuelo, E. Guzmán, F. Ortega, R. G. Rubio, M. A. Rubio, Phase diagram of fatty acid langmuir monolayers from rheological measurements, Langmuir 33 (2017) 4280–4290. URL: https://doi.org/10.1021/acs.langmuir.7b00613. doi:10.1021/acs.langmuir.7b00613. arXiv:https://doi.org/10.1021/acs.langmuir.7b00613, pMID: 28363024.

[56] F. Martínez-Pedrero, J. Tajuelo, P. Sánchez-Puga, R. Chulia-Jordan, F. Ortega, M. Rubio, R. Rubio, Linear shear rheology of aging β-casein films adsorbing at the air/water interface, Journal of Colloid and Interface Science 511 (2018) 12 – 20. URL: http://www.sciencedirect.com/science/article/pii/S0021979717311232. doi:https://doi.org/10.1016/j.jcis.2017.09.092.

[57] S. Vandebril, J. Vermant, P. Moldenaers, Efficiently suppressing coalescence in polymer blends using nanoparticles: role of interfacial rheology, Soft Matter 6 (2010) 3353–3362. URL: http://dx.doi.org/10.1039/B927299B. doi:10.1039/B927299B.

[58] K. Masschaele, B. J. Park, E. M. Furst, J. Fransaer, J. Vermant, Finite ion-size effects dominate the interaction between charged colloidal particles at an oil-water interface, Phys. Rev. Lett. 105 (2010) 048303. URL: https://link.aps.org/doi/10.1103/PhysRevLett.105.048303. doi:10.1103/PhysRevLett.105.048303.

[59] S. Barman, G. F. Christopher, Simultaneous interfacial rheology and microstructure measurement of densely aggregated particle laden interfaces using a modified double wall ring interfacial rheometer, Langmuir 30 (2014) 9752–9760. doi:10.1021/la502329s, pMID: 25068732.

[60] S. E. Rahman, N. Laal-Dehghani, G. F. Christopher, Interfacial viscoelasticity of self-assembled hydrophobic/hydrophilic particles at an air/water interface, Langmuir 35 (2019) 13116–13125. URL: https://doi.org/10.1021/

acs.langmuir.9b02251. doi:10.1021/acs.langmuir.9b02251. arXiv:https://doi.org/10.1021/acs.langmuir.9b02251, pMID: 31539264.

[61] B. Brugger, J. Vermant, W. Richtering, Interfacial layers of stimuli-responsive poly-(n-isopropylacrylamide-co-methacrylicacid) (pnipam-co-maa) microgels characterized by interfacial rheology and compression isotherms, Phys. Chem. Chem. Phys. 12 (2010) 14573–14578. URL: http://dx.doi.org/10.1039/C0CP01022G. doi:10.1039/C0CP01022G.

[62] D. Harbottle, Q. Chen, K. Moorthy, L. Wang, S. Xu, Q. Liu, J. Sjoblom, Z. Xu, Problematic stabilizing films in petroleum emulsions: Shear rheological response of viscoelastic asphaltene films and the effect on drop coalescence, Langmuir 30 (2014) 6730–6738. URL: https://doi.org/10.1021/la5012764. doi:10.1021/la5012764. arXiv:https://doi.org/10.1021/la5012764, pMID: 24845467.

[63] L. Imperiali, K.-H. Liao, C. Clasen, J. Fransaer, C. W. Macosko, J. Vermant, Interfacial rheology and structure of tiled graphene oxide sheets, Langmuir 28 (2012) 7990–8000. URL: https://doi.org/10.1021/la300597n. doi:10.1021/la300597n. arXiv:https://doi.org/10.1021/la300597n.

[64] O. Regev, S. Vandebril, E. Zussman, C. Clasen, The role of interfacial viscoelasticity in the stabilization of an electrospun jet, Polymer 51 (2010) 2611 – 2620. URL: http://www.sciencedirect.com/science/article/pii/S0032386110002880. doi:https://doi.org/10.1016/j.polymer.2010.03.061.

[65] M. M. Castellanos, J. A. Pathak, R. H. Colby, Both protein adsorption and aggregation contribute to shear yielding and viscosity increase in protein solutions, Soft Matter 10 (2014) 122–131. URL: http://dx.doi.org/10.1039/C3SM51994E. doi:10.1039/C3SM51994E.

[66] M. Felix, C. Bascon, M. Cermeño, R. J. FitzGerald, J. de la Fuente, C. Carrera-Sánchez, Interfacial/foaming properties and antioxidant activity of a silkworm (bombyx mori) pupae protein concentrate, Food Hydrocolloids 103 (2020) 105645. URL: http://www.sciencedirect.com/science/article/

pii/S0268005X19322441. doi:https://doi.org/10.1016/j.foodhyd.2020.105645.

[67] A. Jaishankar, V. Sharma, G. H. McKinley, Interfacial viscoelasticity, yielding and creep ringing of globular protein–surfactant mixtures, Soft Matter 7 (2011) 7623–7634. URL: http://dx.doi.org/10.1039/C1SM05399J. doi:10.1039/C1SM05399J.

[68] Z. Xue, A. Worthen, A. Qajar, I. Robert, S. L. Bryant, C. Huh, M. Prodanović, K. P. Johnston, Viscosity and stability of ultra-high internal phase co2-in-water foams stabilized with surfactants and nanoparticles with or without polyelectrolytes, Journal of Colloid and Interface Science 461 (2016) 383 – 395. URL: http://www.sciencedirect.com/science/article/pii/S0021979715301260. doi:https://doi.org/10.1016/j.jcis.2015.08.031.

[69] C. Wu, J. Lim, G. Fuller, L. Cegelski, Quantitative analysis of amyloid-integrated biofilms formed by uropathogenic escherichia coli at the air-liquid interface, Biophysical Journal 103 (2012) 464 – 471. URL: http://www.sciencedirect.com/science/article/pii/S0006349512007758. doi:https://doi.org/10.1016/j.bpj.2012.06.049.

[70] F. Janssen, A. G. Wouters, L. Linclau, E. Waelkens, R. Derua, J. Dehairs, P. Moldenaers, J. Vermant, J. A. Delcour, The role of lipids in determining the air-water interfacial properties of wheat, rye, and oat dough liquor constituents, Food Chemistry 319 (2020) 126565. URL: http://www.sciencedirect.com/science/article/pii/S0308814620304271. doi:https://doi.org/10.1016/j.foodchem.2020.126565.

[71] F. Janssen, A. G. Wouters, Y. Meeus, P. Moldenaers, J. Vermant, J. A. Delcour, The role of non-starch polysaccharides in determining the air-water interfacial properties of wheat, rye, and oat dough liquor constituents, Food Hydrocolloids 105 (2020) 105771. URL: http://www.sciencedirect.com/science/article/pii/S0268005X19327997. doi:https://doi.org/10.1016/j.foodhyd.2020.105771.

[72] J. Niskanen, C. Wu, M. Ostrowski, G. G. Fuller, S. Hietala, H. Tenhu, Thermoresponsiveness of pdmaema. electrostatic and stereochemical effects, Macromolecules 46 (2013) 2331–2340. URL: https://doi.org/10.1021/ma302648w. doi:10.1021/ma302648w. arXiv:https://doi.org/10.1021/ma302648w.

[73] O. Soo-Gun, J. C. Slattery, Disk and biconical interfacial viscometers, Journal of Colloid and Interface Science 67 (1978) 516–525. URL: http://linkinghub.elsevier.com/retrieve/pii/0021979778902424. doi:10.1016/0021-9797(78)90242-4.

[74] P. Erni, P. Fischer, E. J. Windhab, V. Kusnezov, H. Stettin, J. Läuger, Stress- and strain-controlled measurements of interfacial shear viscosity and viscoelasticity at liquid/liquid and gas/liquid interfaces, Review of Scientific Instruments 74 (2003) 4916–4924. URL: http://aip.scitation.org/doi/10.1063/1.1614433. doi:10.1063/1.1614433.

[75] J. M. Lopez, A. H. Hirsa, Coupling of the interfacial and bulk flow in knife-edge viscometers, Physics of Fluids 27 (2015) 042102. URL: http://aip.scitation.org/doi/10.1063/1.4916619. doi:10.1063/1.4916619.

[76] P. A. Rühs, N. Scheuble, E. J. Windhab, R. Mezzenga, P. Fischer, Simultaneous control of ph and ionic strength during interfacial rheology of β-lactoglobulin fibrils adsorbed at liquid/liquid interfaces, Langmuir 28 (2012) 12536–12543. URL: https://doi.org/10.1021/la3026705. doi:10.1021/la3026705. arXiv:https://doi.org/10.1021/la3026705, pMID: 22857147.

[77] P. A. Rühs, L. Böni, G. G. Fuller, R. F. Inglis, P. Fischer, In-situ quantification of the interfacial rheological response of bacterial biofilms to environmental stimuli, PLOS ONE 8 (2013) 1–9. URL: https://doi.org/10.1371/journal.pone.0078524. doi:10.1371/journal.pone.0078524.

[78] S. Pandit, M. Fazilati, K. Gaska, A. Derouiche, T. Nypelö, I. Mijakovic, R. Kádár, The exo-polysaccharide component of extracellular matrix is essential for the viscoelastic properties of bacillus subtilis biofilms, International Journal of Molecular Sciences 21 (2020). URL: https://www.mdpi.com/1422-0067/21/18/6755. doi:10.3390/ijms21186755.

[79] C. O. Klein, A. Theodoratou, P. A. Rühs, U. Jonas, B. Loppinet, M. Wilhelm, P. Fischer, J. Vermant, D. Vlassopoulos, Interfacial fourier transform shear rheometry of complex fluid interfaces, Rheologica Acta 58 (2019) 29–45. URL: https://doi.org/10.1007/s00397-018-01122-y.

[80] A. Torcello-Gómez, J. Maldonado-Valderrama, M. J. Gálvez-Ruiz, A. Martín-Rodríguez, M. A. Cabrerizo-Vílchez, J. de Vicente, Surface rheology of sorbitan tristearate and β-lactoglobulin: Shear and dilatational behavior, Journal of Non-Newtonian Fluid Mechanics 166 (2011) 713 – 722. URL: http://www.sciencedirect.com/science/article/pii/S037702571100084X. doi:https://doi.org/10.1016/j.jnnfm.2011.03.008.

[81] M. E. H. van den Berg, S. Kuster, E. J. Windhab, L. M. C. Sagis, P. Fischer, Nonlinear shear and dilatational rheology of viscoelastic interfacial layers of cellulose nanocrystals, Physics of Fluids 30 (2018) 072103. URL: https://doi.org/10.1063/1.5035334. doi:10.1063/1.5035334. arXiv:https://doi.org/10.1063/1.5035334.

[82] M. Biviano, L. J. Böni, J. D. Berry, P. Fischer, R. R. Dagastine, Interfacial properties of chitosan in interfacial shear and capsule compression, ACS Applied Materials & Interfaces 0 (0) null. URL: https://doi.org/10.1021/acsami.0c11781. doi:10.1021/acsami.0c11781. arXiv:https://doi.org/10.1021/acsami.0c11781, pMID: 32921046.

[83] N. A. Tarazona, R. Machatschek, A. Lendlein, Influence of depolymerases and lipases on the degradation of polyhydroxyalkanoates determined in langmuir degradation studies, Advanced Materials Interfaces 7 (2020) 2000872. URL: https://onlinelibrary.wiley.com/doi/abs/10.1002/admi.202000872. doi:10.1002/admi.202000872. arXiv:https://onlinelibrary.wiley.com/doi/pdf/10.1002/admi.202000872.

[84] K. Mishra, J. Bergfreund, P. Bertsch, P. Fischer, E. J. Windhab, Crystallization-induced network formation of tri- and monopalmitin at the middle-chain triglyceride oil/air interface, Langmuir 36 (2020) 7566–7572. URL: https://doi.org/10.1021/acs.langmuir.0c01195. doi:10.1021/acs.langmuir.0c01195. arXiv:https://doi.org/10.1021/acs.langmuir.0c01195, pMID: 32520568.

[85] Y. C. Ray, H. O. Lee, T. L. Jiang, T. S. Jiang, Oscillatory torsional interfacial viscometer, Journal of Colloid And Interface Science 119 (1987) 81–99. URL: https://linkinghub.elsevier.com/retrieve/pii/0021979787902475. doi:10.1016/0021-9797(87)90247-5.

[86] R. Nagarajan, S. Chung, D. Wasan, Biconical Bob Oscillatory Interfacial Rheometer, Journal of Colloid and Interface Science 204 (1998) 53–60. URL: https://linkinghub.elsevier.com/retrieve/pii/S0021979798955837. doi:10.1006/jcis.1998.5583.

[87] W. Haynes, CRC Handbook of Chemistry and Physics, CRC Handbook of Chemistry and Physics, CRC Press, 2011. URL: https://books.google.es/books?id=pYPRBQAAQBAJ.

[88] K. Takamura, T. G. M. van de Ven, Comparisons of modified effective medium theory with experimental data on shear thinning of concentrated latex dispersions, Journal of Rheology 54 (2010) 1–26. doi:10.1122/1.3263700.

[89] K. Takamura, H. Fischer, N. R. Morrow, Physical properties of aqueous glycerol solutions, Journal of Petroleum Science and Engineering 98-99 (2012) 50–60. URL: http://linkinghub.elsevier.com/retrieve/pii/S0920410512002185. doi:10.1016/j.petrol.2012.09.003.